Rock Physics—The Link Between Rock Properties and AVO Response

J. P. Castagna, M. L. Batzle,‡ T. K. Kan‡*

INTRODUCTION

The variation of seismic reflection amplitude with offset is dependent on intrinsic rock parameters such as compressional-wave velocity (V_p), shear-wave velocity (V_s), density, anisotropy, and attenuation. An understanding of the interrelationships among these parameters and rock properties such as lithology, porosity, and pore fluid content is needed for the quantitative extraction of rock properties information by amplitude variation with offset (AVO) analysis. This paper provides the necessary rock physics framework for AVO analysis.

After briefly discussing some elementary rock physics concepts, we will (1) synthesize available *P*-wave velocity, *S*-wave velocity, and density information; (2) give empirical V_p versus V_s or V_p versus density trend curves for the common sedimentary lithologies; (3) discuss, in detail, the pressure, temperature, and composition dependence of the density and compressibility of pore fluid mixtures of various kinds; (4) demonstrate fluid substitution in rocks using the well known Biot-Gassmann equations and derive the rock skeleton properties needed for these calculations; (5) compile a variety of attenuation measurements including new vertical seismic profiling measurements in a young clastic section; and (6) provide a very basic anisotropy tutorial.

In the course of writing this paper, we have made extensive use of several review papers and books. We have found the following particularly helpful: Gardner et al. (1974), Gregory (1977), White (1983), Thomsen (1986), Simmons (1965), and Töksoz and Johnston (1981).

SOME PRELIMINARIES

Velocity and Elastic Moduli

P- and *S*-wave velocities for an isotropic, homogeneous, elastic material are given by

$$V_p = \left[\frac{k + 4/3\mu}{\rho}\right]^{1/2} \tag{1}$$

and

$$V_s = \left[\frac{\mu}{\rho}\right]^{1/2} \tag{2}$$

where

V_p = compressional-wave velocity,
V_s = shear-wave velocity,
k = rock bulk modulus = rock incompressibility,
μ = rock shear modulus = rock rigidity,

and

ρ = rock bulk density.

Equations (1) and (2) provide the fundamental link between seismic velocities and rock properties. For example, it has been demonstrated many times (e.g., Domenico, 1976, 1977) that the rock bulk modulus may be strongly dependent on the pore fluid bulk modulus while the rock shear modulus may be unaffected by the fluids. Hence, when a compressible free gas replaces liquids in the pore space, the rock *P*-wave velocity will decrease significantly, whereas the rock *S*-wave velocity will be slightly increased due to the decreasing bulk rock density. Consequently, the ratio of compressional-to-shear-wave velocity (V_p/V_s) is expected to be an excellent indicator of free gas in the pore space. This is the basis for direct hydrocarbon detection using AVO.

For a homogeneous isotropic material which is deforming elastically under uniaxial compression, Poisson's ratio (σ) is defined as the negative fractional change in width divided by the fractional change in length (ratio of transverse to axial strain). Poisson's ratio is directly related to the V_p/V_s ratio by

$$\sigma = \frac{.5(V_p/V_s)^2 - 1}{(V_p/V_s)^2 - 1}. \tag{3}$$

*ARCO Oil and Gas Company
‡ARCO Exploration and Production Technology

A Poisson's ratio of zero corresponds to a V_p/V_s ratio of 1.41. Fluids have a Poisson's ratio of .5 (V_p/V_s equals infinity).

Shear modulus is the ratio of shear stress to shear strain. Similarly, bulk modulus is the ratio of volumetric stress to volumetric strain; this is the reciprocal of the compressibility.

Effects of Pressure and Temperature

At a given pressure and temperature, the velocity of a sedimentary rock depends on porosity, lithology, pore fluid content, texture, and lithification. In order to relate velocities to these rock properties, we must first comprehend the environmental effects of pressure and temperature.

Laboratory measurements (for example, Simmons and Brace, 1965) have shown that V_p and V_s for a given rock specimen can vary greatly depending on the confining pressure (P_c) and the pore pressure (P_p).

Numerous laboratory measurements have shown that most rocks obey an "effective stress" law with the "effective" pressure (P_e) given by

$$P_e = P_c - nP_p \quad \text{(with } n \text{ usually equal to 1).} \tag{4}$$

When n is equal to 1, the effective pressure is equal to the "differential pressure" which is the difference between confining and pore pressure. (Terzaghi and Peck; 1948). As shown in Figure 1, the P- and S-wave velocities are functions of the effective pressure. The typical behavior of most porous rocks is for velocities to increase rapidly at low pressure and more slowly at higher pressure. (See Appendix A for pressure units and gradients).

The increase in velocity with pressure is usually attributed to the closing of thin crack-like pores and grain contacts within the rock. In solid materials and rocks without cracks, the velocities stay almost constant with pressure. Figure 2 shows the measured changes in rock volume with pressure which correspond to the velocity changes shown in Figure 1. Since the constituent minerals of the rock are relatively incompressible, the bulk volume change can be assumed to be primarily due to pore volume changes.

The dependence of velocity on effective pressure complicates the establishment of velocity-porosity relationships. Any velocity-porosity transform which does not explicitly include pressure as a variable must be used very cautiously, particularly at low effective pressures.

The direct effect of temperature on V_p and V_s is small when we remain within the ranges commonly encountered in hydrocarbon exploration. Timur (1977) has shown that even for an increase in temperature of 100 degrees Celsius, the velocities drop by only a few percent. According to Nur and Simmons (1969) and DeVilbiss et al. (1978) such changes in velocity are largely due to the effects of temperature on the pore fluids while the skeleton properties remain approximately constant. Larger changes can be expected when high temperatures cause a vapor phase (i.e., steam flooding).

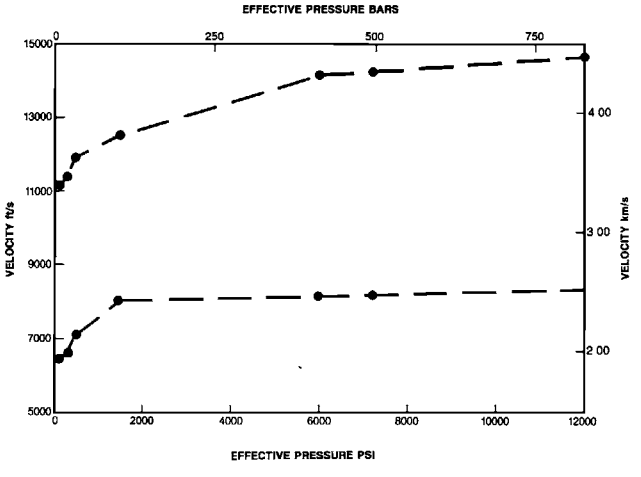

Fig. 1. Variation of P- and S-wave velocity with pressure for a water-saturated glauconitic sandstone with a porosity of 19.2 percent sampled from a depth of 11 833.5 ft (3606.7 m).

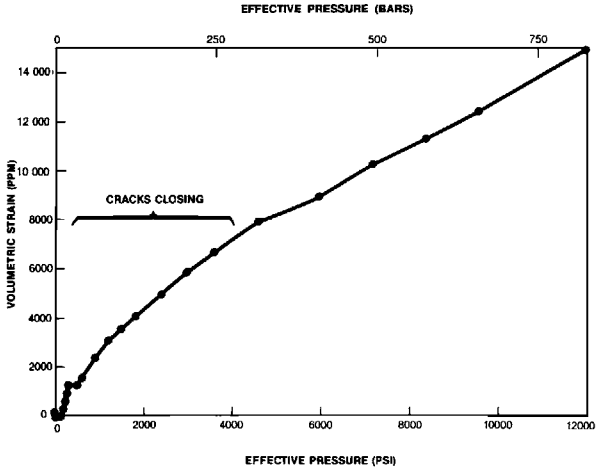

Fig. 2. Variation of volumetric strain with pressure for the sample described in Figure 1.

When we move from the laboratory into real in-situ conditions, the confining pressure becomes the pressure due to the weight of the overburden, which depends on depth and average rock bulk density and is often expressed as a pressure gradient (pressure divided by depth). The overburden (lithostatic or geostatic) pressure gradient is usually assumed to be about .0226 MPa/meter (1.0 psi/ft) for Tertiary deposits off the Texas-Louisiana Gulf Coast. This value corresponds to an average overburden bulk density of 2.31 gm/cc. As shown in Appendix A, the pressure gradient may deviate significantly from this value.

The hydrostatic pressure is the pressure due to the weight of the overlying fluid column. The hydrostatic pressure gradient is usually about .0105 MPa/meter (.465 psi/ft) for typical formation waters but can vary depending on the pore fluid salinities and temperature. In normally pressured rocks, pore pressure is equal to the hydrostatic pressure. However, in geopressured formations, the pore pressure is abnormally high, and effective pressure is abnormally low.

Geothermal gradients range from about 8 to 40 degrees Celsius per kilometer (0.4 to 2.2°F/100 ft.) and are typically around 20 degrees Celsius per kilometer (1.1°F/100 ft.) in many sedimentary basins. The gradients tend to be relatively low in young areas with rapid deposition. The reader is referred to Gretener (1981) for an excellent overview.

The indirect effects of pressure and temperature can be substantially larger than the direct effects discussed thus far. As a rock is buried, the increasing pressures and temperatures produce bulk porosity reduction, phase changes, cementation, and other diagenetic modifications. Bear in mind that exposing a rock to elevated pressures and temperatures in a laboratory does not produce the same result as when the rock is exposed to these conditions over geologic time.

V_P-V_S RELATIONSHIPS

Because rocks are aggregates of mineral grains, we expect the velocity of a highly lithified, low-porosity rock to be strongly dependent on the velocities of the grains. However, we expect the velocity of an unconsolidated rock to be only weakly dependent on the velocities of the grains due to the large pore volume and the influence of pore shape.

Because most sedimentary rock-forming minerals (such as quartz, calcite, and clays) are not isotropic, mineral velocity is taken to be that of a zero-porosity polycrystalline aggregate of randomly oriented mineral grains (Hill, 1952). In general, we expect the velocity of a monomineralic rock to approach the velocity of the pure mineral as porosity approaches zero.

Mineral velocity is generally referred to as the "matrix" velocity in log analysis and the "grain" or "solid" velocity in the rock physics literature. Table 1 gives *P*- and *S*-wave velocities for some minerals commonly found in sedimentary rocks. The *S*-wave velocity for dolomite is not well established. Conspicuously absent from this list are the clay minerals. Some information about clay velocities can be ascertained by extrapolation of measurements on mixed lithologies to 100 percent clay (see Table 2).

When V_p and V_s are crossplotted, we expect, for relatively "pure" (mono-mineralic) water-saturated rocks, the mineral velocity to constitute one endpoint of a distribution of points representing varying porosities and effective pressures. At the other extreme, as the rock becomes more fluid-like and the compressional velocity approaches that of water, we expect the *S*-wave velocity to go to zero. We show that this behavior is indeed exhibited by the common sedimen-

Table 1. Some reported mineral properties. Mineral velocities are averaged to represent zero-porosity isotropic aggregates.

Mineral	Density (gm/cc)	V_p (km/s)	V_s (km/s)	V_p/V_s	Reference*
Calcite	2.71	6.53	3.36	1.94	(1)
Calcite	2.71	6.26	3.24	1.92	(2)
Dolomite	2.87	7.05	4.16	1.70	(3)
Halite	2.16	4.50	2.59	1.74	(4)
Muscovite	2.79	5.78	3.33	1.74	(5)
Quartz	2.65	6.06	4.15	1.46	(2)
Quartz	2.65	6.05	4.09	1.48	(6)
Anhydrite	2.96	6.01	3.37	1.78	(7)

*(1) Dandekar (1968). (2) Anderson and Liebermann (1966), (3) Nur and Simmons (1969), (4) Birch (1966), (5) Aleksandrov and Ryzhova (1961), (6) McSkimin et al. (1965), (7) Rafavich et al. (1984).

Table 2. Some interpreted clay velocities. These data are extrapolations to 100 percent clay from mixed lithologies.

Description	V_p (km/s)	V_s (km/s)	V_p/V_s	Reference*
Mixed clays	3.40	1.60	2.13	(1)
Mixed clays	3.41	1.63	2.09	(2)
Montmorillonite/ illite mixture	3.60	1.85	1.95	(3)
Illite	4.32	2.54	1.70	(4)

*(1) Tosaya (1982), (2) Han et al. (1986), (3) Castagna et al. (1985), (4) Eastwood and Castagna (1986).

tary rocks by crossplotting V_p and V_s for different lithologies.

For the following V_p-V_s crossplots, we combined a variety of our own measurements with data from the literature. We attempted to plot data for only relatively pure lithologies; however, as compositional analyses are usually not reported with published velocity data, it is certain that a good deal of scatter is present due to compositional variations and associated uncertainties.

Figure 3, including the data of Pickett (1963) and Milholland et al. (1980) in addition to our own, shows the V_p-V_s relationship for limestone. For S-wave velocities greater than 1.5 km/s, Pickett's relation of $V_p = 1.9V_s$ holds extremely well. However, as

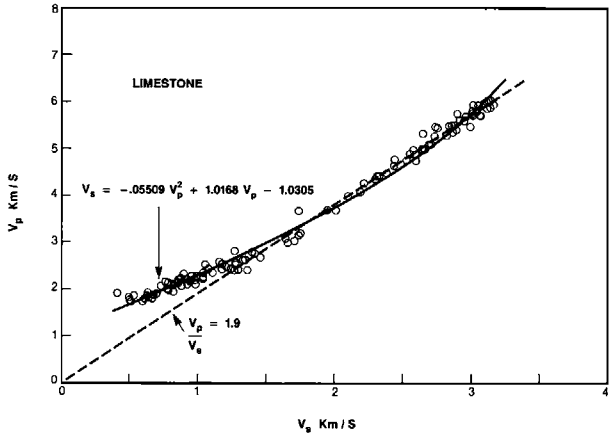

Fig. 3. Crossplot of V_p versus V_s for limestones. The dashed line is Pickett's (1963) trend. The solid line is a second-order polynomial fit to the experimental data.

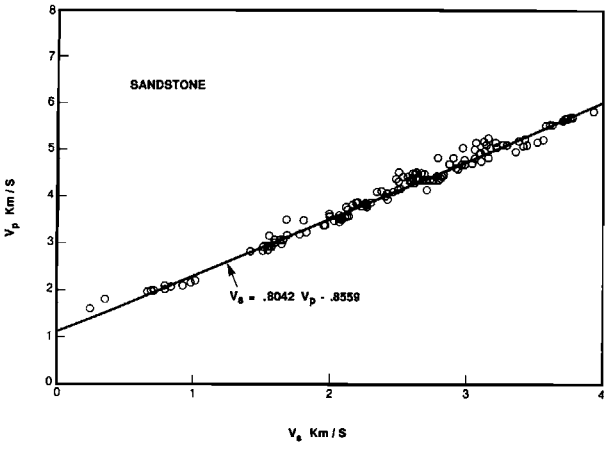

Fig. 4. Crossplot of V_p versus V_s for sandstones. The solid line is the linear regression fit to the experimental data.

hypothesized, at low velocities, there is a substantial deviation from this trend as V_p approaches 1.5 km/s (water velocity) while V_s approaches zero. The least-squares polynomial fit to the data is

$$V_s \text{ (km/s)} = -.05509 \quad V_p^2 + 1.0168 \quad V_p - 1.0305. \tag{5}$$

Note that for V_s greater than 1.5 km/s, Pickett's linear trend is superior to equation (5) which is a better fit for the entire velocity range.

In contrast, V_s is nearly linearly related to V_p over the entire range of data for sandstones and shales (Figures 4 and 5). Included on these plots, in addition to our own data, are data reported in the compilations in Castagna et al. (1985) and Thomsen (1986). The V_p-V_s relationships are

$$V_s \text{ (km/s)} = .8042\ V_p - .8559 \tag{6}$$

for sandstone, and

$$V_s \text{ (km/s)} = .7700\ V_p - .8674 \tag{7}$$

for shale. These trends are similar to the mudrock line obtained exclusively from in-situ measurements in Castagna et al. (1985) given by

$$V_s \text{ (km/s)} = .8621\ V_p - 1.1724, \tag{8}$$

and in close agreement with the results of Han et al. (1986) for 75 sandstone samples,

$$V_s \text{ (km/s)} = .7936\ V_p - .7868. \tag{9}$$

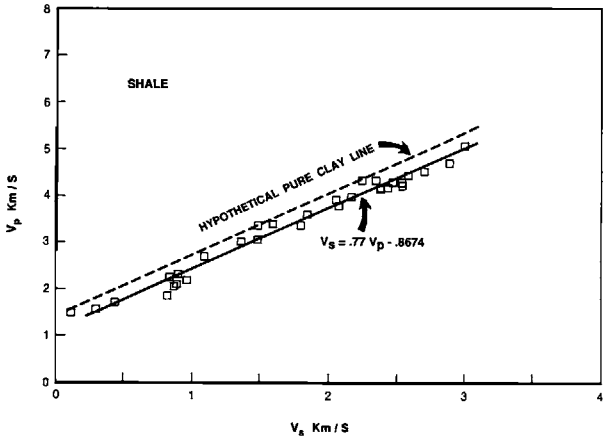

Fig. 5. Crossplot of V_p versus V_s for shales. The solid line is the linear regression fit to the experimental data. The dashed line represents a possible location for a hypothetical pure clay line.

Shale velocities reported in Johnston (1986) fall close to the shale trend of equation (7).

From equations (6) through (9), we may conclude that sandstones and shales exhibit very similar V_p-V_s relationships. If one assumes that the majority of the scatter about these trend curves is due to compositional variation in a binary quartz-clay system, it can be reasoned that a pure clay line would give a slightly higher V_p/V_s ratio than predicted by equation (7). Similarly, a pure quartz line would yield a slightly lower V_p/V_s ratio then given by equation (6). However, pure quartz sands and pure clay shales are scarce, so equations (6) and (7) are preferable for use when compositions are not precisely known; particularly prior to drilling. When estimating S-wave velocities from conventional sonic logs and well log volumetric analyses, slightly modified equations can be used to represent "pure" lithologies. In addition, our experience has shown that feldspathic sands tend to exhibit higher V_p/V_s than do quartzose sandstones.

According to Gregory (1977), gas sands have V_p/V_s ratios of about 1.5. In the laboratory, we have seen ratio variations from under 1.4 to over 1.8 with an average of about 1.5. The effect of gas saturation on V_p/V_s is discussed in greater detail below.

We can report velocity data for dolomites only over a limited range (see Figure 6). Once again, a linear fit is adequate for this range;

$$V_s \text{ (km/s)} = .5832\ V_p - .07776 \qquad (10)$$

which is virtually the same as Pickett's trend $V_p = 1.8V_s$.

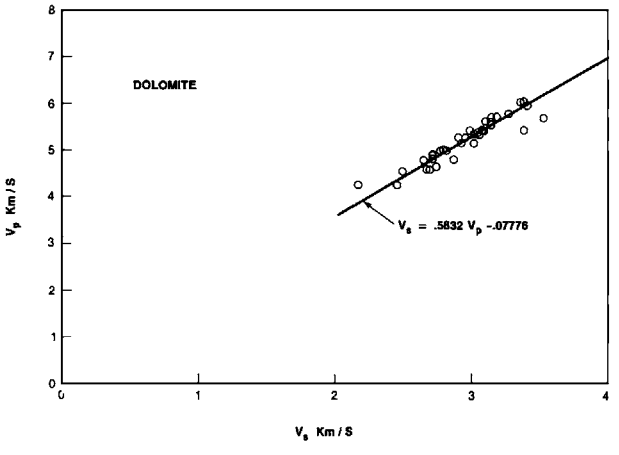

Fig. 6. Crossplot of V_p versus V_s for dolomites. The solid line is a linear regression fit to the experimental data.

Table 3 summarizes the V_p/V_s regressions for limestone, dolomite, sandstone, and shale.

Although our experience with V_p-V_s relationships in coals is limited, we have observed V_p-V_s ratios from about 1.9 to 2.2 in the laboratory. However, these results are biased toward competent samples, and we can expect higher V_p/V_s in low velocity coals (see Appendix B for more data). We have also found V_p/V_s to be about 1.8 for anhydrite and 1.7 for rock salt with relatively little variation due to small porosity variation for these rocks.

Figure 7 shows full-waveform sonic log velocities in a variety of rock types including mixed lithologies. We make the following observations for these data: (1) Clean limestones tend to fall along Pickett's limestone trend ($V_p = 1.9V_s$). (2) Sandstones and shales tend to fall along the mudrock line (equation 8). (3) Salt falls along a limited portion of the mudrock line with V_p about 4.4 km/s and V_p/V_s about 1.7. (4) Dolomites and mixed lithologies fall between the limestone and mudrock lines, and (5) Dolomites tend to have V_p/V_s ratios that are less than predicted by Pickett's dolomite trend ($V_p = 1.8V_s$). This variance may be due to (a) high silica content, or (b) pore shape distribution different from Pickett's dataset.

A composite plot of V_p/V_s relationships (Figure 8) allows us to draw certain conclusions about the use of V_p/V_s ratios to ascertain lithology. Lithology discrimination is best at high velocities where the rule of thumb that V_p/V_s is equal to 1.6 for sandstone, 1.8 for dolomite, and 1.9 for limestone is most nearly correct. In this region, however, it is difficult to distinguish high velocity shales from carbonates. Furthermore, the experimental error associated with extracting V_p/V_s ratios for seismic data will be large compared to the differences in V_p/V_s due to lithology variation. At high velocities, the difference in V_p/V_s between gas- and brine-saturated rocks will be relatively small. For low velocity rocks, lithology discrimination is also difficult; however, the difference in V_p/V_s between gas and brine saturated rocks will be relatively large. As a consequence, AVO analysis for hydrocarbons will be more robust for lower velocity targets.

VELOCITY-DENSITY RELATIONSHIPS

Bulk rock density (ρ_b) is directly related to mineral (matrix) density and porosity by

$$\rho_b = (1 - \phi)\rho_{ma} + \phi\rho_f \qquad (11)$$

where

ϕ = porosity,

ρ_{ma} = matrix (grain) density,

and

ρ_f = pore fluid density.

The lithology affects bulk density through the matrix density parameter (ρ_{ma}). In mixed lithologies, this is taken to be the volume weighted average grain density.

Densities of minerals commonly found in sedimentary rocks are given in Table 4. We give the idealized formula for each mineral, and the density reported in Johnson and Olhoeft (1984) which represents the most commonly accepted density for each mineral. This density may not necessarily correspond to the exact chemical formula given. Furthermore, in recognition of variations due to cation substitution, non-stochiometric components, and impurities, we give a range of reported densities for which we have also drawn from Hurlbut (1971) and/or Judd and Shakoor (1981). In contrast, we also present clay mineral densities commonly used in well log analysis in Table 5 (Schlumberger, 1986). Note that these densities are consistently less than the clay densities given in Table 4. It is likely that the densities used in log analysis contain some contributions from excess water bound between clay layers or onto clay surfaces, and/or tied up in microporosity. For seismic modeling purposes, care must be taken in choosing the appropriate grain density; when total porosity is given (i.e., total water volume) Table 4 provides the correct grain densities (in practice, 2.65 gm/cc is a convenient choice for "shale" grain density). However, when effective porosity is used, Table 5 gives the appropriate grain density for clays.

Velocity-density relationships can be obtained from the velocity-porosity transforms which are used in well log analysis. The best known velocity-porosity transform is the Wyllie et al. (1956) time-average equation (WGG equation) given by

$$1/V_p = (1 - \phi)/V_{pma} + \phi/V_f \qquad (12)$$

where

V_p = compressional wave velocity,
V_{pma} = grain ("matrix") compressional wave velocity, and
V_f = fluid compressional wave velocity.

Obviously, this relationship could also be written in terms of density if the grain and fluid densities were known.

The WGG equation is often used in well consoli-

Table 3. $V_p - V_s$ regression coefficients for various lithologies. Coefficients are for equations of the form: $V_s = aV_p^2 + bV_p + C$.

Lithology	Limestone	Dolomite	Sandstone	Shale
a	−0.05508	—	—	—
std err	0.00616	—	—	—
b	1.01677	0.58321	0.80416	0.76969
std err	0.04780	0.03736	0.00899	0.02039
c	−1.03049	−0.07775	−0.85588	−0.86735
std err of Y est	0.08783	0.10421	0.10603	0.11981
R squared	0.99096	0.87444	0.98352	0.97939
# observations	129	37	136	32

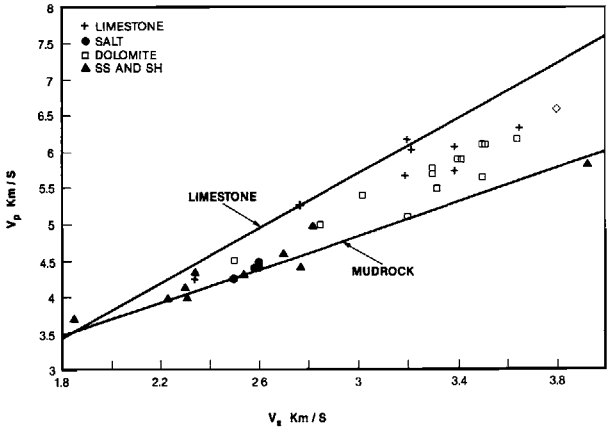

Fig. 7. Crossplot of V_p versus V_s for full waveform sonic log data. The mudrock line is from Castagna et al. (1985). The limestone line is from Pickett (1963).

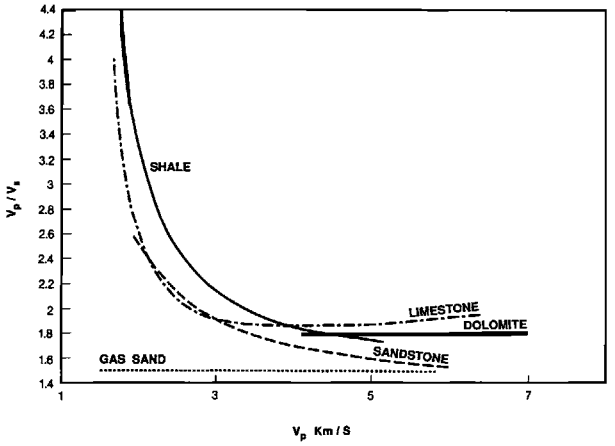

Fig. 8. V_p/V_s versus V_p trends for various lithologies. For water-saturated rocks V_p/V_s approaches infinity as V_p approaches fluid velocity.

dated sandstones for porosity determination from well logs. The equation can be easily derived by assuming that the wave propagates for a fraction of its time in the "matrix",

$$(1 - \phi)/V_{pma}$$

and a fraction of its time in the fluid,

$$\phi/V_f.$$

This is not a physically correct representation of wave propagation in porous media (as it is strictly valid only at wavelengths which are much smaller than the grain/pore size), but is a convenient means of deriving the form of the equation. One should resist the temptation to attach physical meaning to V_f, particularly in gas sands where the use of gas velocities can give erroneous results. This equation also tends to break down where the effective stress is low and where the rock is poorly consolidated. Under these circumstances a "compaction factor" is applied to correct the time-average porosity prediction.

An "improvement" to the time-average equation was proposed in Raymer et al. (1980). According to the Raymer-Hunt-Gardner (RHG) equation:

$$V_p = (1 - \phi)^2 V_{pma} + \phi V_f. \qquad (13)$$

Raymer et al. (1980) claim that this equation for sands and sandstones is valid for porosities less than 37 percent. The RHG equation is also empirical in nature, and may not be applicable in all circumstances. As with the WGG equation, the RHG equation must be corrected for low effective stress and poor consolidation.

Table 4. Densities of minerals commonly found in sedimentary rocks. these data are commonly accepted values although variations exist due to cation substitution, non-stochiometric components, and impurities (from Johnson and Olhoeft, 1984; Hurlbut, 1971; and Judd and Shakoor, 1981).

Mineral	Formula	Density	Reported Range gm/cc
Kaolinite	$Al_2Si_2O_5(OH)_4$	2.594	(2.59–2.68)
Montmorillonite	$(Na, K, Mg, Ca)_{.33}(Al, Mg)_2Si_4O_{10}(OH)_2 \cdot nH_2O$	2.608	(2–3?)
Chlorite	$Mg_3(Si_4O_{10})(OH)_{12} \cdot Mg_3(OH)_6$	2.800	(2.6–3.3)
Illite	$(H, K)_3Al_8(Si, Al)_{16}O_{40}(OH)_8$	2.660	(2.6–2.9)
Glauconite	$K_{1.5}(Fe^{3+}, Mg, Al, Fe^{2+})_{4-6}(Si, Al)_8O_{20}(OH)_4$	2.3	highly variable
Muscovite	$KAl_3Si_3O_{10}(OH)_2$	2.831	(2.7–3.0)
Biotite	$K_2(Mg, Fe)_{4-6}(Si, Al)_8O_{20}(OH)_4$	2.900	(2.7–3.3)
Quartz	SiO_2	2.648	—
Feldspar	$KAlSi_3O_8$ (Microcline-Orthoclase)	2.56–2.57	(2.55–2.63)
	$NaAlSi_3O_8$ (Albite)	2.62	—
	$CaAl_2Si_2(OH)_8$ (Anorthite)	2.76	—
Calcite	$CaCO_3$	2.710	—
Dolomite	$CaMg(CO_3)_2$	2.866	(2.82–2.87)
Siderite	$FeCO_3$	3.944	—
Pyrite	FeS_2	5.011	(4.95–5.03)
Gypsum	$CaSO_4 \cdot 2H_2O$ (Alabaster)	2.305	—
Anhydrite	$CaSO_4$	2.963	—
Halite	NaCl	2.163	(2.04–2.17)
Iron Oxides		—	(5.200–5.275)
Iron Hydroxides		—	(3.1–4.0)
Zeolites		—	(2.0–2.4)

Table 5. Suggested matrix densities for well log interpretation (Schlumberger Log Interpretation Chartbook, 1986).

Mineral	Formula	Density (gm/cc)
Kaolinite	$Al_4Si_4O_{10}(OH)_8$	2.41
Chlorite	$(Mg, Fe, Al)_6(Si, Al)_4O_{10}(OH)_8$	2.76
Illite	$K_{1-1.5}Al_4(Si_{7-6.5}Al_{1-1.5})O_{20}(OH)_4$	2.52
Montmorillonite	$(Ca, Na)_7(Al, Mg, Fe)_4(Si, Al)_8O_{20}(OH)_4(H_2O)_N$	2.12

Castagna (1985) used Biot-Gassmann theory (Gassmann, 1951; Biot, 1956) to derive an S-wave RHG-like equation for sandstones:

$$V_s = (1 - \phi)^2 V_{sma} \tag{14}$$

where V_{sma} is the matrix S-wave velocity. It is satisfying to note that this equation can also be derived by replacing V_{pma} with V_{sma} and setting $V_f = 0$ in equation (13).

For unconsolidated sediments, Raymer et al. (1980) used a derivative of the Wood (1941) equation for suspensions. The Wood equation is

$$1/K_{su} = \sum_{i=1}^{n} \frac{X_i}{K_i} \tag{15}$$

where

K_{su} = suspension bulk modulus,
X_i = volume fraction of component i,
K_i = bulk modulus of component i, and
n = number of components including fluids and solids.

The Wood-like equation used in Raymer et al. (1980) accounts for some development of frame rigidity by using the plane-wave modulus rather than the bulk modulus of the solid:

$$1/M = (1 - \phi)/M_{ma} + \phi/K_f \tag{16}$$

where

M = bulk rock plane-wave modulus = $k + 4/3\mu$,
M_{ma} = solid grain plane-wave modulus, and
K_f = fluid bulk modulus.

One of the most important empirical reactions in seismic prospecting is the Gardner et al. (1974) equation which expresses density in terms of velocity for an average of all rock types:

$$\rho_b = 1.741\ V_p^{.25} \tag{17a}$$

where V_p is expressed in km/s, or

$$\rho_b = .23\ V_p^{.25} \tag{17b}$$

where V_p is expressed in ft/s, and density is given in gm/cc.

Unlike the WGG and RHG equations, the Gardner equation is fit to a very wide range of velocities and porosities and thus implicitly accounts for variations in consolidation and effective stress. Figure 9 compares the Gardner equation to laboratory and well log velocity and density data for sandstones and shales. The Gardner equation tends to overestimate density for sandstones and underestimate density for shales. Lithologic variation can be taken into account by using different Gardner equations for each lithology. These are given in Table 6 and were obtained by least-squares fits to digitized curves from Gardner et al. (1974), with the exception of the sandstone equation which was modified to approach the quartz point at low porosities.

In contrast to V_p/V_s relationships, V_p-density relationships are not well defined. This is amply demonstrated by Figure 10 which compares the different velocity-density relationships for sandstone including: (1) the WGG equation, (2) the RHG equation, (3) the Wood-like equation, (4) the Gardner equation, (5) the Gardner sandstone equation, and (6) the modified Gardner sandstone equation. Figure 11 is a crossplot of a sampling of laboratory and well log data for sandstones. The RHG and Wood-like equations tend to act as upper and lower limits for velocity at a given density, while the modified Gardner sandstone equation provides the best fit to the data; although this can be characterized as a rough fit at best. Similarly, the velocity-density crossplot for various shales (Figure 12) shows a great deal of scatter. When an arbitrary "pure clay" endpoint is selected, RHG and Wood-like equations again provide approximate upper and lower limits for velocity at a given density. The Gardner shale equation provides the most reasonable fit to the data, but deviations from this trend can be large. Similar conclusions may be drawn for the other lithologies; thus, when a rough velocity-density transform is required, we recommend the Gardner equations summarized in Table 6 and Figure 13. When more precise estimates are required, however, it will be necessary to explicitly consider effective stress and consolidation or to develop local empirical trends.

As velocity variation with pressure is typically greater than the porosity variation with pressure, velocity-porosity relationships should also vary with pressure. Domenico (1984) developed velocity-porosity relationships at different effective pressures for the sandstone and limestone measurements of Pickett (1963) and showed that the porosity dependence of velocity is greater at low effective stress. In the following discussion, for a wide range of data, we are unable to demonstrate any statistically significant relationship between pressure and the magnitude of the porosity dependence of velocity.

MIXED LITHOLOGIES

In the majority of situations, the explorationist must deal with lithologies that are mixed to some degree, rather than pure. Hence, we require methods for averaging the properties or relationships developed for pure rock types. Examples of averaging schemes include the Voigt-Reuss and Hashin-Shtrikman bounds (see Watt et al., 1976, for an excellent review). Unfortunately, these bounds may not be sufficiently tight for our applications. An alternative approach is composite media modeling assuming a solid with inclusions having specific shapes and elastic properties [for example, the Kuster-Töksoz (1974) and the O'Connell-Budiansky (1974) models]. Unfortunately, existing models require accurate and detailed information about the rock fabric before any calculations can be made. They also make assumptions (such as pore non-interaction) that have not been generally demonstrated to hold for sedimentary rocks. Consequently, it is necessary, once again, to resort to empirical equations.

A time-averaging approach is commonly taken in well log analysis by modifying the WGG equation to include the effects of composition. A "clay correc-

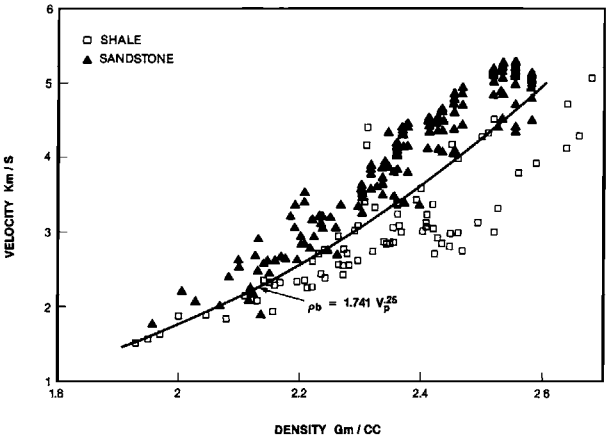

Fig. 9. Laboratory and log measurements for sands and shales showing Gardner's relation. (Gardner et al., 1974).

Table 6. Second-order polynomial fits to the Gardner et al. (1974) velocity-density relationships. The sandstone trend has been modified to approach the quartz point at low porosities. Units are km/s and gm/cc.

(a) Coefficients for the equation. $\rho = aV_p^2 + bV_p + c$

Lithology	a	b	c	V_p Range (Km/s)
Shale	−.0261	.373	1.458	1.5–5.0
Sandstone	−.0115	.261	1.515	1.5–6.0
Limestone	−.0296	.461	.963	3.5–6.4
Dolomite	−.0235	.390	1.242	4.5–7.1
Anhydrite	−.0203	.321	1.732	4.6–7.4

(b) Coefficients for the equation $\rho = dV_p^f$

Lithology	d	f	V_p Range (Km/s)
Shale	1.75	.265	1.5–5.0
Sandstone	1.66	.261	1.5–6.0
Limestone	1.50	.225	3.5–6.4
Dolomite	1.74	.252	4.5–7.1
Anhydrite	2.19	.160	4.6–7.4

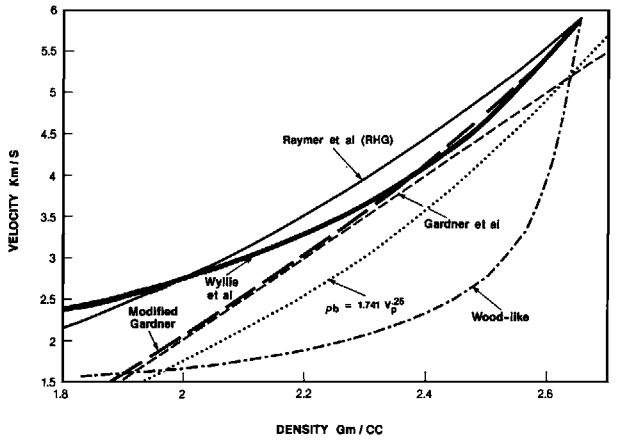

Fig. 10. Sandstone velocity-density trend curves. Light solid line—Raymer et al. (1980); heavy solid line—Wyllie et al. (1956); medium dashed line—modified Gardner (see text); dotted line—Gardner et al. (1974) for sedimentary rocks; dot-dashed line—Wood-like equation (see text).

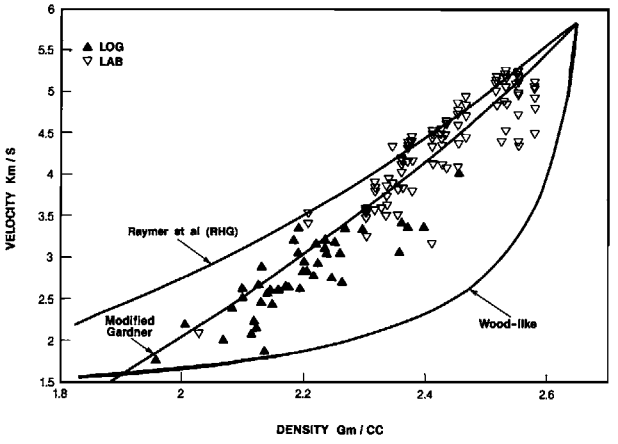

Fig. 11. Sandstone laboratory and log measurements.

tion" utilizing the fractional volume of clay, "X_{cl}", and an assumed clay matrix velocity, "V_{cl}", (see Table 2) is often used. The modified WGG equation can be written:

$$1/V_p = X_{cl}/V_{cl} + X_{ss}/V_{ss} + \phi/V_f \qquad (18)$$

where

X_{ss} = volume of sandstone

and

V_{ss} = matrix velocity for sandstone

Similarly, terms may be added for other lithologic components.

A number of authors (mentioned in the following discussion) have presented similar equations which are, however, linear in velocity, rather than linear in the reciprocal of velocity (transit-time or slowness) as is the WGG equation.

Tosaya (1982) performed ultrasonic velocity measurements on brine-saturated sands and shales at 5800 psi. Clay contents were obtained by thin-section microscopy, X-ray diffraction, and elemental analysis. Multiple regression was used to derive the relationships between P- and S-wave velocity and porosity and clay content.

These equations are

$$V_p \text{ (km/s)} = 5.8 - 8.6\phi - 2.4X_{cl} \qquad (19a)$$

and

$$V_s \text{ (km/s)} = 3.7 - 6.3\phi - 2.1X_{cl} \qquad (19b)$$

where

V_p = P-wave velocity,
V_s = S-wave velocity,
ϕ = fractional porosity,

and

X_{cl} = fractional volume of clay.

Kowallis et al. (1984) performed ultrasonic velocity measurements on dry poorly consolidated sandstones. Clay contents were obtained by thin-section microscopy, X-ray diffraction, SEM observation, and elemental analysis. Multiple regression yielded:

$$V_p \text{ (km/s)} = 5.6 - 9.2\phi - 5.7X_{cl}. \qquad (20)$$

Castagna et al. (1985) performed multiple regression on full-waveform sonic log measurements in the geopressured Frio formation at a depth of about 16 000 ft. Porosity and clay volume were determined by neutron-density crossplot calibrated by the X-ray diffraction data of Freed (1980). This yielded equations which are very similar to those of Tosaya (1982):

$$V_p \text{ (km/s)} = 5.81 - 9.42\phi - 2.21X_{cl} \qquad (21a)$$

and

$$V_s \text{ (km/s)} = 3.89 - 7.07\phi - 2.04X_{cl}. \qquad (21b)$$

Han et al. (1986) performed the most thorough examination of this kind for sandstones. They made ultrasonic velocity measurements on 75 different sandstones. Clay contents were obtained by point counting. Their equations for a number of different pressures are given in Table 7. Eberhardt-Phillips et al. (1989) fit these data with the following equations:

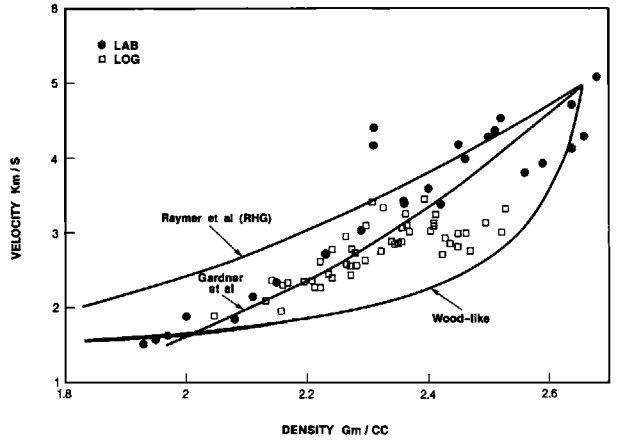

Fig. 12. Shale laboratory and log measurements.

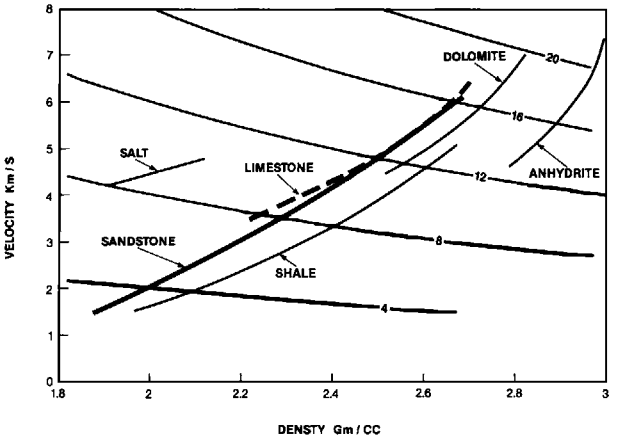

Fig. 13. Velocity-density trends from Gardner et al. (1974) and lines of constant impedance. Impedance units are (km-gm)/(cc-s).

$$V_p = 5.77 - 6.94\phi - 1.73\sqrt{X_{cl}} + .446(P - e^{-16.7P}) \quad (22a)$$

$$V_s = 3.70 - 4.94\phi - 1.57\sqrt{X_{cl}} + .361(P - e^{-16.7P}) \quad (22b)$$

where P is the effective stress is kilobars.

Wilkens et al. (1984) and Rafavich (1984) performed lithological regressions on carbonates and evaporites. Rather than review their results separately, these data are incorporated into the following regression analysis.

In an attempt to unify the previously mentioned measurements and other data into one "global" set of equations, we have selected 972 measurements from the literature and our own database for analysis. These measurements were selected on the basis of the following criteria:

(1) specimen was fully water-saturated;
(2) composition was determined by x-ray diffraction, point count, or wet chemical analysis;
(3) both P- and S-wave velocity measurements were available; and
(4) composition was limited to the quaternary system quartz-clay-dolomite-calcite.

Velocities were assumed to be a composition-weighted linear average of the porous end-member lithologies:

Table 7. Sandstone velocity regressions by Han et al, (1986). Coefficients are for the equation $V = a + b\phi + cX_{cl}$ where ϕ equals porosity and X_{cl} equals clay volume fraction.

Effective Stress (bars)	P-Wave Velocity		
	a	b	c
400	5.59	−6.93	−2.18
300	5.55	−6.96	−2.18
200	5.49	−6.94	−2.17
100	5.39	−7.08	−2.13
50	5.76	−7.08	−2.02
Effective Stress (bars)	S-WaveVelocity		
	a	b	c
400	3.52	−4.91	−1.89
300	3.47	−4.84	−1.87
200	3.39	−4.73	−1.81
100	3.29	−4.73	−1.74

$$V = \sum X_i V_i = \sum X_i(A_i\phi + B_i \log P + C_i) \quad (23)$$

where P is the effective stress, X_i is the volume fraction of each component, i, V_i are the velocities of pure quartz, clay, calcite, and dolomite aggregates at the given porosity and pressure and

$$\sum X_i = 1. \quad (24)$$

Multiple linear regression yielded the coefficients given in Table 8. Residual analysis revealed no compelling nonlinearities or other obvious inadequacies in equation (23).

In particular, such improvements as (1) nonunity exponent for X_{cl}, (2) A_i a function of pressure, (3) B_i a function of porosity, and (4) pressure dependence different from log P (see Eberhardt-Phillips et al., 1989) did not significantly improve the residual error. This is presumably because the effects described are masked in this dataset by experimental error (primarily in composition). One should keep in mind that equation (23) is a significant improvement over the Tosaya-Han-Nur and Eberhardt-Phillips-Zoback forms in one respect: the porosity and pressure coefficients are lithology dependent.

Analysis of the coefficients given in Table 8 provides some very interesting insights.

(1) For compressional waves, the pressure dependence (partially described by B_i log P) is independent of lithology. For S-waves, the effect is lithology dependent. In both cases, the pressure dependence is the same for clay and quartz.
(2) For P-waves, the porosity dependence is the same for clay and quartz.
(3) For P-waves, items (1) and (2) indicate that the regressions presented by previous authors without lithology dependent porosity and pressure coefficients are valid for quartz-clay mixtures. However, for carbonates and for S-wave velocities, lithology dependence of the coefficients is required.
(4) Setting P = 500 bars and ϕ = 0, reasonable matrix velocities are obtained (see Table 9). Notable discrepancies from expected mineral velocities are (a) very low V_p/V_s(1.41) for zero-porosity clay, and (b) low V_p and V_s for dolomite. These deviations may indicate inadequacies in the regression model (equation 23) or our database.

Overall, the equations presented are consistent with our expectations. Velocity is most strongly dependent

on porosity, with clay content being the next most important factor. When mineral properties are similar, we expect little variation with composition. Hence, the conclusion in Rafavich et al. (1984) that mineralogy only plays a secondary role.

For the equations presented in this section, the reader should be aware of a number of potential problems:

(1) The "independent variables" may be highly correlated, so the coefficients may be misleading.
(2) The equations are forced to be linear. Although this is generally adequate, problems may arise at times (e.g., according to Han et al. (1986), the effect of adding a small amount of clay to a sandstone can be nonlinear).
(3) The equations only apply to the specific effective pressure range for which the measurements were made.
(4) The use of a "volume clay" term ignores the variability of clay mineralogy and structural role.
(5) Variations in lithification, texture, and pore geometry are ignored.
(6) The pressure dependence is probably not adequately described.
(7) The effect of pressure may be exaggerated (at low effective stress) by sample damage.

Consequently, local independent confirmation of these equations with in-situ measurements (well logs) is desirable.

FLUID PROPERTIES

This section summarizes work which is more fully described in Batzle and Wang (1992). The pore fluids we are concerned with consist of three primary types: hydrocarbon gases, hydrocarbon liquids (oils), and

Table 8. Velocity regression coefficients for the system quartz-clay-calcite-dolomite: Equation $V = \Sigma X_i(A_i\phi + B_i \log P + C_i)$.

Coefficient	P	S
A_{quartz}	−7.636 ± .125	−4.691 ± .141
B_{quartz}	.192 ± .016	.166 ± .013
C_{quartz}	5.289 ± .0466	3.156 ± .035
A_{clay}	−7.636 ± .125	−12.655 ± 1.049
B_{clay}	.192 ± .016	.166 ± .013
C_{clay}	2.708 ± .059	1.844 ± .135
$A_{calcite}$	−10.136 ± .278	−5.429 ± .236
$B_{calcite}$	.192 ± .061	.068 ± .014
$C_{calcite}$	5.818 ± .039	3.156 ± .035
$A_{dolomite}$	−4.765 ± .444	−4.692 ± .141
$B_{dolomite}$	.192 ± .061	.137 ± .010
$C_{dolomite}$	5.524 ± .062	3.156 ± .035
Correlation Coefficient (R)	.969	.946
R^2	.940	.895
Standard Error	.220	.171
F	2143.687	1179.008
Signif F	.000	.000

Note: Coefficients are all significant (i.e., significance of $T \approx 0$). Velocities are in km/s and pressures are bars. Identical coefficients indicate that no statistically significant difference was found for an initial regression trial, and parameters were lumped for the final regression.

Table 9. Extrapolated velocities at zero porosity and 500 bars effective pressure. Units of velocity are km/s.

Mineral	Extrapolated V_p	Extrapolated V_s	Extrapolated V_p/V_s	Measured V_p	Measured V_s	Measured V_p/V_s
Quartz	5.81	3.60	1.61	6.06	4.12	1.47
Clay	3.23	2.29	1.41	—	—	—
Calcite	6.34	3.34	1.90	6.40	3.30	1.94
Dolomite	6.04	3.52	1.72	7.05	4.16	1.70

brines. The situation is complicated since we are dealing with substances of variable compositions. The hydrocarbons form a continuum of light to heavy compounds ranging from almost an ideal gas to almost solid organic residues. Brines can range from nearly pure water to saline solutions of nearly 50 percent salt. In addition, gases will be dissolved in both the oils and brines and will dramatically alter the velocities. Finally, we must also be concerned with mixtures of distinct phases since reservoirs usually have substantial brine saturations.

Gas

The gas phase is the easiest to characterize. The compounds are usually relatively simple and the thermodynamic properties have been thoroughly examined. Hydrocarbon gases usually consist of the light hydrocarbons of methane, butane, propane, etc. Additional gases, such as water vapor and heavier hydrocarbons, will occur in the gas depending on the pressure, temperature, and history of the deposit. The specific weight of these gases, as compared to air at standard temperature and pressure, will vary from about 0.6 for nearly pure methane to over 1.5 for gases with heavier components. Fortunately, when a rough idea of the gas weight is known, a fairly accurate estimate can be made of the gas properties at pressure and temperatures. Thomas et al. (1970) did a very complete analysis of the acoustic properties of natural gases and we will follow a similar analysis here.

The important seismic characteristics of a fluid (the bulk modulus, density, and sonic velocity) are all related to primary thermodynamic properties. Hence for gases we are obliged to start with the ideal gas law.

$$PV = nRT \tag{25}$$

where P is pressure, V is volume, n is the number of moles of the gas, R is the gas constant, and T the absolute temperature. This leads to a density ρ, of

$$\rho = \frac{nM}{V} = \frac{MP}{RT} \tag{26}$$

where M is the molecular weight. The isothermal compressibility β_T is

$$\beta_T = \frac{-1}{V}\left[\frac{\partial V}{\partial P}\right]_T \tag{27}$$

for compressibility defined as a positive number.

If we calculate the "isothermal" velocity V_T we find

$$V_T^2 = \frac{1}{\beta_T \rho} = \frac{RT}{M}. \tag{28}$$

Hence, velocity would go up with temperature and be independent of pressure.

A pair of mitigating factors must now be considered to bring the relationship closer to reality. First, since there are rapid temperature changes associated with the passage of an acoustic wave, we must use the adiabatic compressibility, β_s, rather than the isothermal compressibility.

$$\gamma \cdot \beta_S = \beta_T. \tag{29}$$

Here, γ is the ratio of heat capacity at constant pressure to the heat capacity at constant volume. In most solid materials, the difference between the isothermal and adiabatic compressibilities is negligible. However, in fluid phases, particularly gases, the isothermal compressibility can be twice the adiabatic value.

The second, more obvious factor stems from the inadequacies of the ideal gas law, equation (25). The gas law can be corrected by adding a compressibility factor (z). The relationships are thus modified

$$PV = znRT, \tag{30}$$

$$\rho = MP/zRT, \tag{31}$$

and

$$\beta_S = \beta_T/\gamma = M/(\gamma \rho z RT). \tag{32}$$

The heat capacity ratio can itself be derived if the equations of state of the material are known. The seismic characteristics of the gas can, therefore, be described if we have an adequate description of z with pressure, temperature, and composition.

Thomas et al. (1970), made use of the Benedict-Webb-Rubin (BWR) equation to define the gas behavior. The BWR equation of state is a rational equation with numerous constants based on the behavior of natural gas mixtures. These gas mixtures range in gravity G (relative to air) from about 0.5 to 1.8. The results of the density calculations are shown in Figure 14. As would be expected, the gas densities increase with pressure and decrease with temperature. However, the densities are also strongly dependent on the gas gravity which is composition dependent.

The adiabatic gas modulus K_s (the inverse of β_s) is also strongly dependent on the composition as well as the pressure and temperature conditions. Figure 15 shows the calculated modulus from the Thomas relationships. Again, the modulus increases with pressure

and decreases with temperature but the relationship is not as linear. The impact of variable composition (gravity) is again obvious.

Oil

Crude oils can be mixtures of extremely complex organic compounds. Natural oils range from the lightest condensate liquids of low carbon number to very heavy tars. At the heavy extreme are bitumen and kerogen which may be denser than water and act essentially like solids. At the light extreme are condensates which may become gas with decreasing pressure. Oils can absorb large quantities of hydrocarbon gases under pressure, thus significantly decreasing the moduli. Under room conditions, the densities can vary from 0.5 gm/cc to greater than 1 gm/cc with most produced oils in the 0.7 to 0.8 gm/cc range. The American Petroleum Institute (API) number N_{API}, is defined as

$$N_{API} = \frac{141.5}{\rho} - 131.5. \tag{33}$$

This results in API numbers of about 5 for very heavy oils to near 100 for light condensates. The extreme variations in composition and ability to absorb gases produce greater variations in the seismic properties of oils.

If we have a general equation of state for oils we could calculate the moduli and densities as we did for the gases. Such equations abound in the petroleum engineering literature. Unfortunately, the equations are almost always strongly dependent on the exact composition of a given oil. In exploration, we normally only have a rough idea of what the oils may be like. In some reservoirs, individual yet adjacent zones will have quite distinct oil types. We will, therefore, proceed along rather empirical lines based on the density of the oil.

The acoustic properties of numerous organic fluids have been studied as a function of pressure or temperature (see, for example, Rao and Rao, 1959). Generally, if we stay away from phase boundaries, the velocities, densities, and moduli are quite linear with pressure and temperature. In organic fluids typical of crude oils, the moduli decrease with increasing temperature and increase with increasing pressure. Wang and Nur (1986) did an extensive study of several light alkanes, alkenes, and cycloparaffins and found simple relationships among the density, moduli, temperature, and carbon number or molecular weight. For velocity they found

$$V_T = V_o - b\Delta T \tag{34}$$

where V_o is the initial velocity, V_T the velocity at temperature T, ΔT is the temperature change and b is a constant for each compound of molecular weight M:

$$b = 0.306 - 7.6/M. \tag{35}$$

Similarly, the velocities are related in molecular weight by

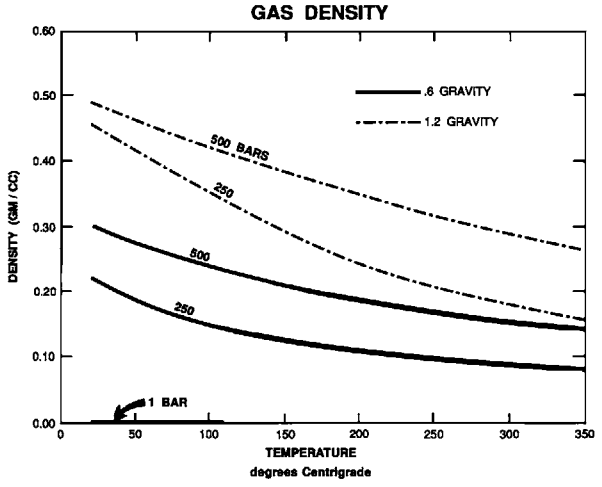

Fig. 14. Hydrocarbon gas density as a function of temperature pressure and composition. Densities are plotted for a light gas (0.6 gravity) and heavy gas (1.2 gravity) at 1, 250, and 500 bars. The two lines overlay at 1 bar.

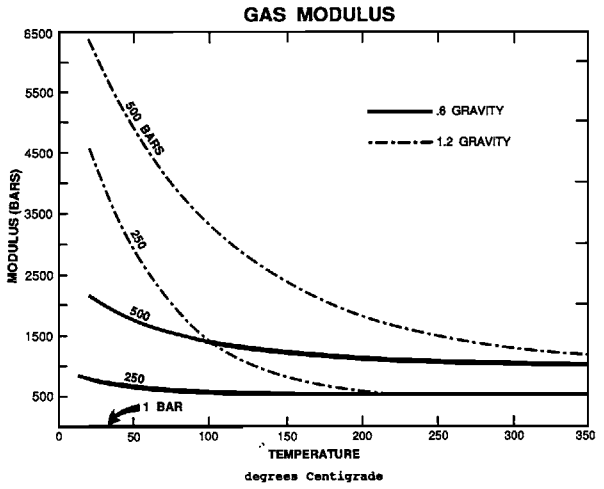

Fig. 15. Gas modulus at pressure and temperature. As in Figure 14, the values for the light and heavy gasses overlay at 1 bar.

$$V_{TM} = V_{TOMO} - b\Delta T - a_m\left[\frac{1}{M} - \frac{1}{M_o}\right] \quad (36)$$

where V_{TM} is the velocity of oil of weight M and V_{TOMO} is the velocity of a reference oil of weight M_o at temperature T_o. The variable a_m is a positive function of temperature. We can see from the rightmost term in equation 36 that the velocity of the fluid will increase with increasing molecular weight. When compounds are mixed, Wang and Nur (1986) found that the resulting velocity is a simple fractional average of the end components. This is roughly equivalent to a fractional average of the bulk moduli of the end components. Pure simple hydrocarbons, therefore, behave in a simple predictable way. We need to extend this analysis to include crude oils which are generally much heavier and have more complex compositions. The influence of pressure must also be determined. In the petroleum engineering literature, broad empirical relationships are available. By empirically fitting equations to these data we can get density as functions of initial density (or API number), temperature, and pressure

$$\rho = F(\rho_0, T, P). \quad (37)$$

These densities are shown in Figure 16.

By differentiating equation (37) we obtain the isothermal compressibility β_I

$$\beta_I = \frac{1}{\rho}\left[\frac{\partial \rho}{\partial P}\right]_T. \quad (38)$$

If we assume a reasonable and constant heat capacity ratio γ, of 1.15 (Wang, personal communication) we obtain the adiabatic bulk moduli K_s,

$$K_S = \frac{\gamma}{\beta_I} = \frac{\gamma\rho}{\left[\frac{\partial \rho}{\partial P}\right]_T} \quad (39)$$

The ultrasonic velocities of a variety of crude oils measured recently are reported in Wang et al. (1988). A general relationship of oil velocity was derived.

$$V = 15\ 454(77.1 + \text{API})^{-1/2} - 1.14T + 0.462P - (1.146 \times 10^{-3} - 4.13 \times 10^{-4}\ \text{API}^{1/2})TP \quad (40)$$

where V is in m/s, T in °C, P in bars, and API is the API degree of the oil, or

$$V = 215 + 50700(77.1 + \text{API})^{-1/2} - 6.72T + (.1096 - 0.00166\ \text{API}^{1/2})P - (1.44 \times 10^{-4} - 5.18 \times 10^{-5}\ \text{API}^{1/2})TP \quad (41)$$

for V in ft/s, T in degrees F, and P in psi.

Using these velocities and the densities as shown in Figure 16, we get the moduli shown in Figure 17.

Very large amounts of gas or light hydrocarbons can go into solution in crude oils. In fact, the lighter crudes are condensates from the gas phase. We would expect the "live" or gas-saturated oils to have significantly different properties than the "dead" or gas-free oils commonly available and measured. The amount of gas that can be dissolved is a function of pressure, temperature, and the composition of both the gas and the oil (Standing, 1962).

$$R = 0.1266G[P \cdot \exp(.02878N_{\text{API}} - 0.00378T)]^{1.205} \quad (42)$$

where R is the gas-oil ratio in liters/liter (1 liter/liter = 5.615 cu ft/BBL) at atmospheric pressure and at 15.5°C and G is the gas gravity. Equation (42) indicates that much larger amounts of gas can go into the light (high API number) oils. In fact, heavy oils may precipitate heavy compounds if much gas goes into solution.

The effect of this gas in solution on the oil acoustic properties has not been well documented. Sergeev (1948) noted that gas in solution will reduce both oil and brine velocities. He calculated that this mix would change some reservoir reflection coefficients by more than a factor of two. A rough estimate of this dissolved gas effect can be made by assuming that the relationship in equation (40) remains valid and by adjusting the oil density to include the gas component. We are assuming here that the gas is a liquid component with its own volume and density and that the result is an ideal liquid mixture. The simple additive relations found in Wang and Nur (1986) support this concept. The estimated density becomes

$$\rho_G = \rho_0(0.972 + 0.000147F^{1.175}) \quad (43)$$

where ρ_0 is the dead oil density and ρ_G is the gas saturated live oil density. The factor F is derived from the gas/oil ratio

$$F = R\left[\frac{G}{\rho_0}\right]^{1/2} + 75. \quad (44)$$

Figure 18 shows the live and dead oil velocities measured in Wang et al. (1988) along with the estimates using equations (40), (42), and (43).

Brines

The great bulk of the pore fluids consists of brines. Their composition can range from almost pure water to saturated saline solutions. Figure 19 shows the salt concentrations found in brines from several wells from Arkansas and Louisiana. Gulf of Mexico area brines often have rapid increases in concentration with increasing depth. In other areas, California for example, the concentrations are usually lower but can vary drastically between adjacent fields.

The thermodynamic properties of aqueous solutions have been studied in detail. Kennan et al. (1969) give a relation for pure water that can be iteratively solved to give densities at pressure and temperature. Helgeson and Kirkham (1974) use this and other data to calculate a wide variety of water properties over an extensive temperature and pressure range. One obvious effect of salinity is to increase the density of the fluid. Rowe and Chou (1970) presented a polynomial to calculate both specific volume and compressibility of various salt solutions at pressure over a limited temperature

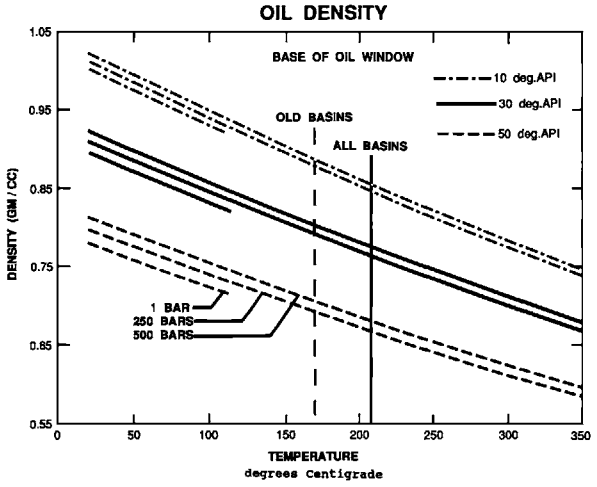

Fig. 16. Oil density as a function of pressure, temperature, and initial API gravity. Three constant-pressure lines are plotted for each oil weight. The 1 bar line is restricted because of phase instability at low pressures and high temperatures. The base of the oil window is represented for old basins (dashed vertical line) and all basins (solid vertical line).

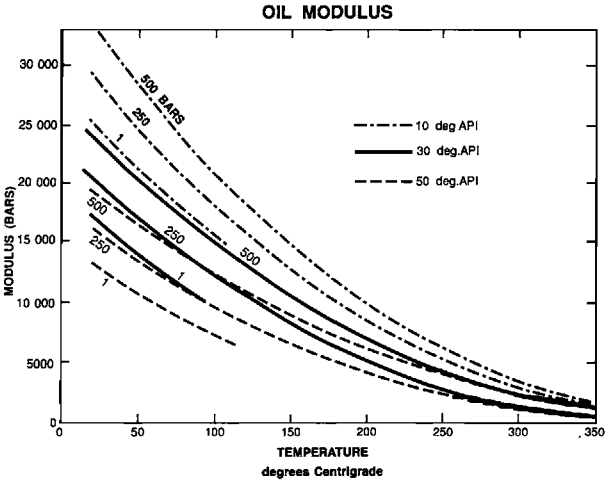

Fig. 17. Oil modulus as a function of pressure temperature, and initial gravity.

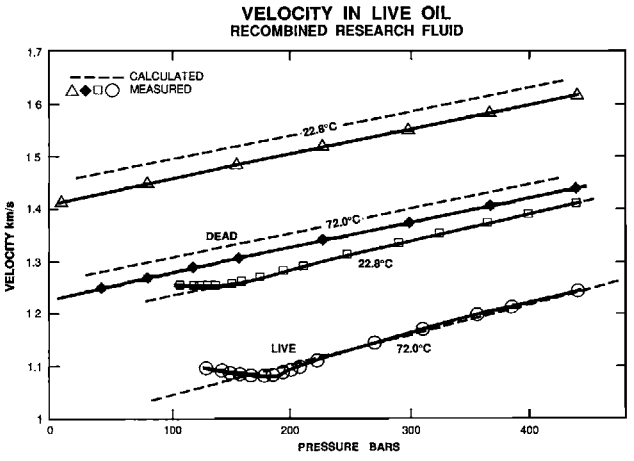

Fig. 18. Measured acoustic velocity of oil both "live" or gas saturated, and "dead" without gas. Measurements were made at 22.8 and 72.0 degrees centigrade. At about 200 bars, gas begins to come out of solution from the live oil. The dashed lines are the calculated velocities.

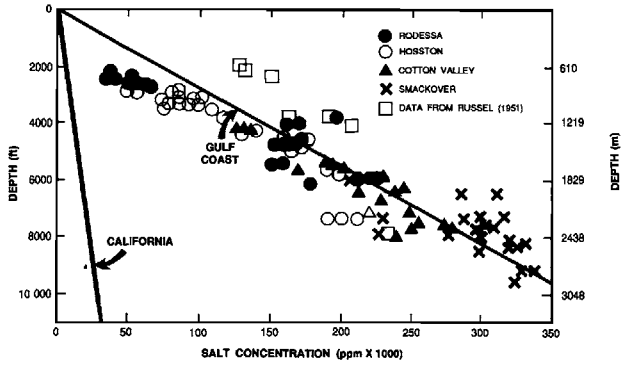

Fig. 19. Salt concentration in sand waters versus depth in southern Arkansas and northern Louisiana after Dickey (1986).

range. Extensive additional data on sodium chloride solutions is provided in Zarembo and Fedorov (1975) and Potter and Brown (1977). Utilizing all these data, a simple polynomial can be constructed that will adequately calculate the density of sodium chloride solutions:

$$\rho_W = \sum_{i=0}^{4} \sum_{J=0}^{2} a_{ij} T^i P^j \qquad (45a)$$

and

$$\rho_B = \rho_W + \sum_{i=0}^{2} \sum_{j=0}^{2} \sum_{k=1}^{2} b_{ijk} T^i P^j x^k. \qquad (45b)$$

Here T and P are in degrees centigrade and bars respectively, x is the weight fraction of sodium chloride, ρ_B is the density of the brine in gm/cm^3. The constants a_{ij} are given in Table 10. The calculated brine densities, along with selected data from Zarembo and Federov, 1975 are plotted in Figure 20. The accuracy of this relationship is limited largely to the extent that other mineral salts, particularly divalent ions, are in solution.

A vast amount of acoustic data is available for brines, but generally for pressure, temperature, and salinity expected under oceanic conditions. Wilson (1959) provides a relationship for the velocity V_w, of pure water to 100°C and about 1000 bars

$$V_W = \sum_{i=0}^{4} \sum_{j=0}^{3} W_{ij} T^i P^j \qquad (46)$$

where the constants W_{ij} are given in Table 10. Millero et al. (1977) and Chen et al. (1978) give additional factors to be added to the velocity of water to calculate

Table 10. Coefficients for water density and modulus computation.

Water Density		Brine Density		Brine Velocity	
a00	0.9999786094	b001	6.683493 E−01	c00	1174.617 E+00
a10	4.463057 E−06	b101	8.981443 E−05	c10	−9.5739 E+00
a20	−5.666686 E−06	b201	2.616639 E−07	c20	5.9847 E−02
a30	1.732672 E−08	b002	4.367547 E−01	c30	−1.1431 E−04
a40	−2.891463 E−11	b102	−3.489720 E−03	c40	4.6486 E−08
a01	4.886269 E−05	b202	1.193570 E−05	c01	2.6337 E−01
a11	−2.217865 E−05	b011	6.864324 E−05	c11	−2.8892 E−04
a21	3.121667 E−09	b111	−2.034837 E−06	c21	−1.7427 E−07
a31	−1.264349 E−11	b211	8.432142 E−09	c30	0
a41	2.325326 E−14	b012	−2.423939 E−04	c40	0
a02	−3.334526 E−09	b112	4.656608 E−04		
a12	−2.404481 E−11	b212	−2.222059 E−09	c12	7.0642 E−09
		b022	−5.509494 E−08	c22	−2.3951 E−11
		b122	1.242326 E−09	c32	0
		b222	−5.091158 E−12	c42	0
Water Velocity				c03	5.2362 E−09
w00	1402.8505963			c13 to c43	0
w10	4.871385 E+00				
w20	−4.782846 E−02			d00	7.8760 E+02
w30	1.487149 E−04			d20	−7.5164 E−04
w40	−2.197453 E−07			d10	−4.2250 E−01
w01	1.523600 E−01				
w02	3.436930 E−05			d11	1.2715 E−04
w03	−1.186670 E−08			d21	−1.0739 E−07
w11	−1.110884 E−03			d02	1.6102 E−03
w21	2.746744 E−05			d12	0
w31	−6.503402 E−08			d22	0
w41	7.986792 E−11				
w12	1.739250 E−06			e0	−8.24262 E+02
w22	−2.135126 E−08			e1	9.5602 E−01
w32	−1.454887 E−10			e2	−1.5012 E−03
w42	5.230233 E−13				
w13	−1.628460 E−09				
w23	1.237155 E−11				
w33	1.326619 E−13				
w43	−4.613582 E−16				

the effects of salinity. Their corrections, unfortunately, are limited to 55°C and 1 molal ionic strength (55 000 ppm). We can extend their results by utilizing the data of Wyllie et al. (1956) to 100°C and 150 000 ppm NaCl. Still, this leaves the high temperature and pressure region with no data. Here we can use the isothermal modulus calculated from equation (45) to estimate the adiabatic moduli. We can also utilize the velocity function provided in Chen et al. (1978) but with the constants modified to fit the additional data. The heat capacity ratio for the brine can be estimated from the PVT relationship in equation (45) and estimates of the isobaric heat capacity from Helgeson and Kirkham (1974):

$$B = m \sum_{i=0}^{4} \sum_{j=0}^{3} c_{ij} T^i P^j + m1.5 \sum_{i=0}^{2} \sum_{J=0}^{2} d_{ij} T^i P^j + m^2 \sum_{i=0}^{2} e_i P^i \qquad (47a)$$

and

$$V_B = V_W + B. \qquad (47b)$$

In this equation, m is the molal salt concentration and c_{ij}, d_{ij}, and e_i are constants given in Table 10.

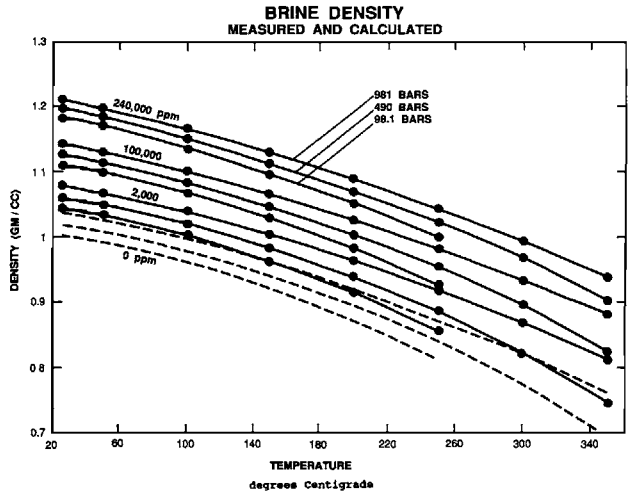

Fig. 20. Brine density as a function of pressure, temperature, and salinity. Symbols are data of Zarembo and Fedorov, 1975; Solid lines are regression fits to these data; Dashed lines are regression fits for pure water.

The calculated moduli using equations (45) and (47) are shown in Figure 21.

Gas can also go into solution with the brine. The amount of gas in solution is substantially less than for the light oils. However, sufficient gas can be in solution in some deep brines for them to be considered an energy resource. Culberson and McKetta, 1951; Sultanov et al., 1972; Brill and Beggs, 1977; and others have shown that the amount of gas that will go into solution increases with pressure and decreases with salinity. The effect of temperature is less substantial. Dodson and Standing (1945) found that the solution's isothermal modulus K_G, decreased almost linearly with gas content:

$$K_G = K_B/(1 + 0.0494\ g) \qquad (48)$$

where g is the gas/water ratio at standard pressure and temperature. Equation (48) shows that for a reasonable gas/water ratio of 10 liters/liter (at room pressure and temperature) the isothermal modulus will be reduced by a third. We presume that the adiabatic modulus will be similarly affected. Assuming this to be true, brine modulus versus gas-water ratio plots are provided in Appendix C. The effect of dissolved gas on density is negligible.

GASSMANN'S EQUATIONS

A variety of theoretical models have been developed to predict the velocities of porous media. In broad terms, the models developed for isotropic rocks fall into two categories: (1) pore geometry specific, and (2) global. Well known examples of geometry specific models include the O'Connell-Budiansky (1974) and

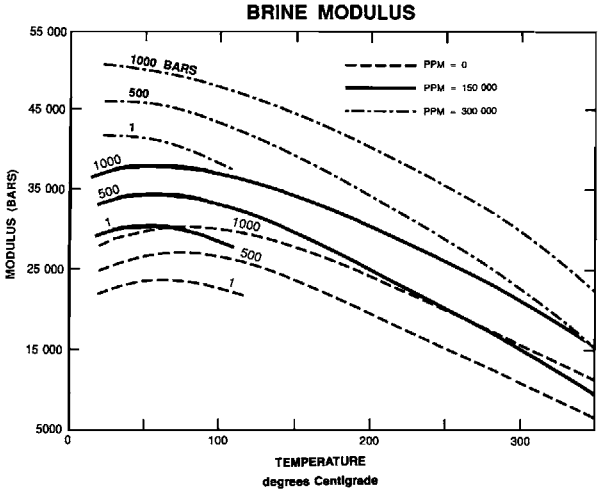

Fig. 21. Calculated brine modulus as a function of pressure, temperature, and salinity.

Kuster-Toksoz (1974) models. These models require the assumption of dilute distributions of idealized pores and have not been shown to be generally applicable to sedimentary rocks. Mavko and Nur (1977) demonstrated that the results can be strongly dependent on the assumed pore shape. Application of these models using the observed pore characteristics has proved difficult at best (Hadley, 1976).

More applicable results have been obtained using the global or bulk properties of the rocks and fluids without referring to any specific pore geometry. Gassmann (1951) and Biot (1956) produced fundamental and yet relatively simple relationships where the most significant unknown parameters are the bulk and shear moduli of the rock framework (skeleton). Gassmann's equations are valid only at low (seismic) frequencies (strictly valid at zero frequency). These are (Domenico, 1976)

$$k_w = k_d + (1 - b)^2/[(1 - \phi - b)/k_{ma} + \phi/k_f] \quad (49)$$

and

$$\mu_w = \mu_d \quad (50)$$

where

k_w = bulk modulus of the fluid filled rock,
k_d = bulk modulus of rock skeleton (aggregate of grains),
k_{ma} = bulk modulus of matrix (individual grains),
k_f = bulk modulus of pore fluid,
$b = k_d/k_{ma}$,
μ_w = shear modulus of the fluid filled rock, and
μ_d = shear modulus of rock skeleton.

Often, the skeleton bulk modulus is unknown but the bulk modulus of the fluid-filled rock is easily derived. For example, if V_p at 100 percent water saturation is known for a given lithology, then the V_p-V_s trend curves can be used to obtain V_s. Given V_p, V_s, and density, we obtain the fluid filled moduli from:

$$k_{100\%} = \rho_{100\%}\left(V_p^2 - \frac{4}{3}V_s^2\right) \quad (51)$$

and

$$\mu_{100\%} = \rho_{100\%}\, V_s^2 \quad (52)$$

where the density and moduli are for water saturation of 100 percent.

Once the fluid-filled bulk modulus is known, it is possible to compute the skeleton bulk modulus from:

$$k_d = bk_{ma} \quad (53)$$

where

$$b = (XY - 1)/(X + Y - 2), \quad (54)$$

$$Y = 1 + \phi(k_{ma}/k_f - 1), \quad (55)$$

and

$$X = k_{100\%}/k_{ma}. \quad (56)$$

Once the skeleton bulk modulus is known, it is possible to calculate the fluid-filled modulus for any combination of fluids. The bulk modulus of a fluid mixture will vary with saturation (or liquid fractions) according to Wood's equation. For example in a gas-water system

$$k_f = (k_{\text{water}}k_{\text{gas}})/(k_{\text{gas}}S_{\text{water}} + k_{\text{water}}S_{\text{gas}}) \quad (57)$$

where

k_{water} = water bulk modulus,
k_{gas} = gas bulk modulus,
S_{water} = fractional water saturation, and
S_{gas} = fractional gas saturation = $1 - S_{\text{water}}$.

Given the fluid-filled moduli from equations (51) and (52), all that is required to compute the fluid-filled velocity is the density. For a gas-water system, the density is given by:

$$\rho_b = (1 - \phi)\rho_{\text{ma}} + S_{\text{water}}\phi\rho_{\text{water}} + S_{\text{gas}}\phi\rho_{\text{gas}} \quad (58)$$

where ρ_{ma}, ρ_{water}, and ρ_{gas} are the grain (matrix), water, and gas densities. P- and S-wave velocities can then be obtained from equations (1) and (2).

Figure 22 shows example velocity-saturation curves for a well consolidated porous sandstone. For the case of gas-water mixtures, the introduction of a minor amount of gas causes a large drop in compressional velocity. This is the well known "bright spot" effect which is due to the large drop in pore fluid modulus when a small amount of gas is added. Increasing gas saturation further has the effect of increasing the velocity, because the fluid bulk modulus remains essentially unchanged and the density decreases. For the case of oils, the change in velocity is less dramatic. Light oils cause the velocity to decrease, while very heavy oils can result in a velocity increase.

There has been some debate in the literature concerning the applicability of Gassmann's equations to partially saturated sandstones. In particular, the laboratory measurements of Gregory (1976) and Domenico (1976) do not agree with Gassmann's equations. However, Murphy (1982) has shown that low-frequency laboratory measurements are in accord with Gas-

smann's equations for water saturations above a few percent. On the other hand, measurements made at sonic and ultrasonic frequencies deviate significantly from Gassmann's equations, exhibiting a much more gentle drop in compressional velocity as gas is added to a fully water saturated rock. Inhomogeneous distribution of gas bubbles within the pore space may also cause deviations from Gassman's equations.

Conventional sonic logs generally operate at a frequency of about 10 KHz. In light of Murphy's experimental data, we would expect sonic gas sand velocities to be higher than seismic velocities. Furthermore, the radius of investigation of the sonic tool may not extend beyond the invaded zone around a borehole, where gas is flushed back or dissolved by drilling fluid. Thus, the sonic log response to gas will depend on the amount of residual gas in the flushed zone. This residual can also result in an overestimation of the gas sand velocity.

Sandstone V_p-V_s trends and Gassmann's equations imply a distinct relationship between brine-sand compressional velocity and gas-sand compressional velocity. This issue is discussed in Appendix E.

FRAME MODULI

Ideally, rock frame (skeleton) moduli should be the same for fluid-saturated rocks and dry rocks. In practice, however, some difference could result from chemical and physical interaction between the pore fluid and the solid grains. At low pressures, frame moduli for moist sandstones are less than frame moduli for dry sandstones (e.g., Murphy, 1982). However, this effect has not been demonstrated to be generally significant at typical formation effective stresses. For shaly rocks, there is the possibility of frame moduli modification due to interaction between pore fluids and clay minerals. This effect is also not yet well understood.

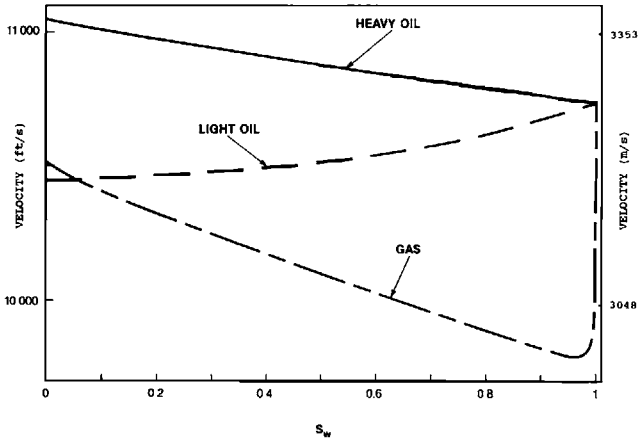

Fig. 22. Calculated velocity versus water-saturation for a typical well-consolidated sandstone.

If there is a difference between dry and wetted frame moduli, the wetted frame moduli should be used for fluid substitution calculations. These can be obtained through Gassmann's equations as described in the previous section. However, if one wishes to calculate frame moduli for high-frequency laboratory data, Gassmann's equations are not adequate. Biot's theory includes the entire frequency range up to the point where the grain scattering becomes important and the rocks can no longer be considered homogeneous; Gassmann's equations are the low frequency limit of Biot's more general relationships. The infinite frequency Biot equations may be more applicable for ultrasonic measurements (see Domenico, 1976):

$$V_p = \left[K_D + \frac{4}{3}\mu + \frac{\dfrac{\phi\rho_b}{\kappa\rho_f} + (1-b)(1-b-2\phi/\kappa)}{(1-\phi-b)/K_{ma} + \phi/K_f} \frac{1}{\rho_b\left[1 - \dfrac{\rho_f\phi}{\rho_b\kappa}\right]}\right]^{1/2} \tag{59}$$

$$V_s = \left[\frac{\mu}{\rho_b\left[1 - \dfrac{\rho_f\phi}{\rho_b\kappa}\right]}\right]^{1/2} \tag{60}$$

where the new parameter, κ, has been introduced. This is the mass coupling factor which varies between 1 (no fluid-solid coupling) and infinity (perfect coupling). For the case of the perfect coupling these equations reduce to the zero frequency case [equations (1), (2), (49), and (50)].

We can study the relationships between saturated frame moduli by deriving bulk and shear moduli from fully water saturated laboratory data using equations (59) and (60). Figures 23a, 23b and 23c are bulk versus shear frame moduli crossplots for dry sandstones, fully-saturated sandstones assuming perfect coupling, and fully-saturated sandstones assuming no coupling. For the case of dry sandstones, dry bulk and shear moduli are about equal. This is consistent with observations in Gregory (1977) and Castagna et al. (1985). When perfect coupling is assumed, the fully saturated frame bulk modulus is greater than the frame shear modulus. However, when no coupling is assumed the frame bulk and shear moduli are again equal. At the

ultrasonic frequencies of laboratory measurements, there should be relatively little fluid-solid coupling. We conclude that, for both dry and saturated laboratory sandstone data, frame bulk and shear moduli are about equal. This corresponds to a frame V_p/V_s ratio of about 1.5. Frame moduli relationships for various lithologies derived in this way are given in Table 11.

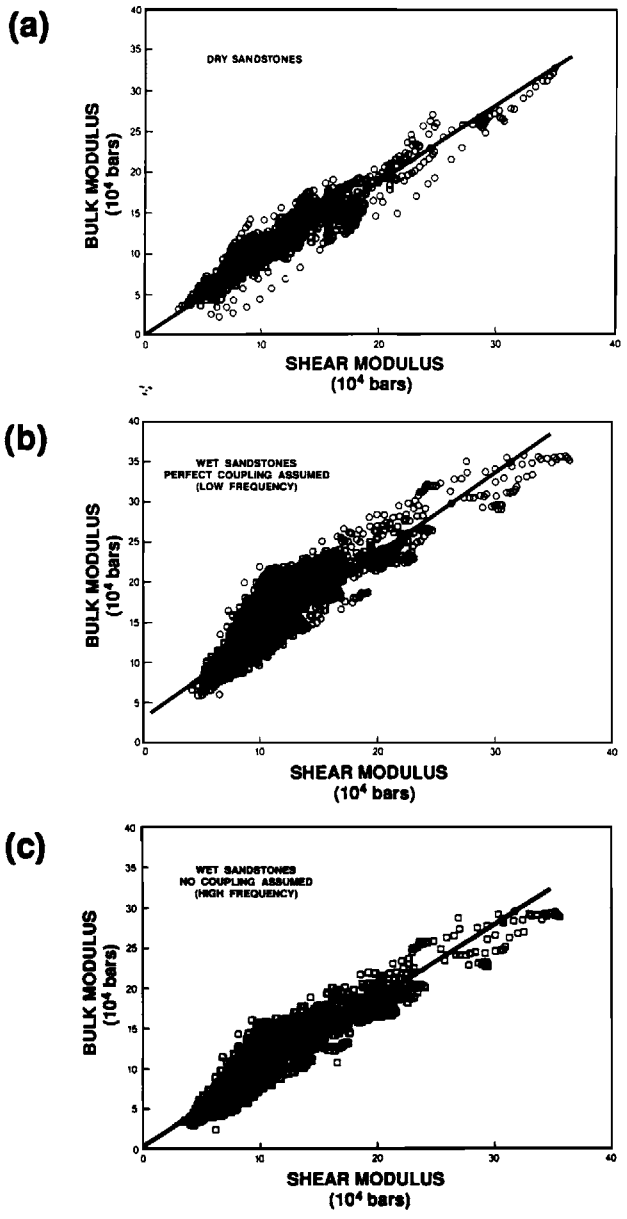

Fig. 23. Skeleton bulk modulus versus shear modulus for (a) dry sandstones, (b) wet sandstones with perfect rock-fluid coupling assumed, (c) wet sandstones with no rock-fluid coupling assumed.

ATTENUATION

Due to increasing path length with offset, overburden attenuation influences seismic amplitude variation with offset. This is most significant for highly attenuating overburdens resulting from poor consolidation or partial gas saturation. Extremely high attenuation in gas reservoirs may also affect AVO, although this effect is expected to be more subtle due to small variations in target zone path length with offset.

The attenuation of a seismic plane wave is described by

$$A(z) = A(0)e^{-\alpha z} \tag{61}$$

where

$A(z)$ = the amplitude of the signal as a function of position z,
$A(0)$ = initial amplitude, and
α = attenuation coefficient.

The attenuation coefficient is related to the quality factor (Q) by:

$$\alpha = \frac{\pi f}{QV} \tag{62}$$

where

f = frequency, and
V = velocity.

Typically, to measure the attenuation coefficient, amplitudes are measured at two locations. The ratio of these amplitudes eliminates the initial amplitude dependence.

$$A(z_1)/A(z_2) = e^{-\alpha(z_1/z_2)}. \tag{63}$$

Hence,

$$\alpha = \frac{\ln [A(z_1)/A(z_2)]}{(z_2 - z_1)} \tag{64}$$

It is generally assumed that, over the seismic frequency band, the quality factor (Q) is constant. This is generally supported for P-waves by spectral ratio measurements which indicate that the attenuation coefficient is linearly proportional to frequency (McDonal et al., 1958). This requires that the product Q times velocity be constant (see equation 62). Since velocity varies only slightly with frequency, Q is approximately constant over the seismic band.

Laboratory measurements above the normal seismic range (e.g., Spencer, 1981; Murphy, 1982) have

shown, however, that over a broad frequency band, Q is strongly frequency dependent. In particular, attenuation peaks between seismic and sonic log frequencies (Figure 24). This effect is most pronounced for partial water saturations.

Figure 25 shows VSP attenuation measurements obtained with a spectral ratio method described in Kan et al. (1983) in a South Texas clastic section. One interval, corresponding to a known gas reservoir, exhibits anomalously high attenuation. This is consistent with laboratory observations (Murphy, 1982).

Table 12 summarizes various in-situ attenuation measurements made in clastic sediments and rocks. There appears to be some tendency toward higher attenuation in sands than in shales, however, the systematics are not at all clear at this time. For example, Anderson and Castagna (1984) observed higher full waveform sonic P-wave attenuation in Frio formation geopressured shales than in adjacent sandstones. The reader is cautioned that in situ measurements of Q tend to be unreliable. These measurements are commonly plagued by such factors as differential frequency dependent coupling, scattering, and narrow bandwidth.

Laboratory evidence indicates that microscopic fluid flow in sandstones is the most important attenuation mechanism. We have already seen how the Biot-Gassmann relationships are modified for the frequency-dependent fluid coupling factor. Winkler (1986) uses these relationships to compare low frequency velocities to ultrasonic laboratory data. Biot (1962), Jones and Nur (1983), Bulau et al. (1984), and Jones (1986) among others have examined how the porosity, permeability, and specific fluid properties will control attenuation and dispersion. Currently, this is a topic of intensive research.

ANISOTROPY

In anisotropic materials, the velocities of P- and S-waves are dependent on the direction of propagation. Furthermore, for S-waves, the velocity may also depend on the polarization of the wave. In AVO analysis, there is the concern that anisotropy of the rocks above and in the vicinity of the target (particularly in shales) will influence the AVO response.

Sedimentary rocks generally exhibit transverse isotropy for which two of the three orthogonal propagation directions are equivalent. For propagation perpendicular to bedding, transverse anisotropy exhibits one P-wave speed and one S-wave speed. For propagation parallel to bedding there are three wave speeds: compressional, horizontally polarized shear, and vertically polarized shear. The vertically polarized shear wave propagating parallel to bedding has the same speed as the vertically propagating shear-wave.

The P-wave anisotropy (E) is defined as:

$$E = (V_{ppa} - V_{ppe})/V_{ppe} \tag{65}$$

where

V_{ppa} = compressional velocity parallel to bedding, and
V_{ppe} = compressional velocity perpendicular to bedding.

Similarly, the shear-wave anisotropy G is defined as

$$G = (V_{spa} - V_{spe})/V_{spe} \tag{66}$$

where

V_{spa} = horizontally polarized shear-velocity parallel to bedding, and
V_{spe} = shear-velocity perpendicular to bedding.

Table 11. Frame moduli relationships derived from fully-saturated ultrasonic velocity measurement assuming no fluid-solid coupling and Biot's high frequency equations. Units are in bars.

Lithology	Equation
Limestone	$k = 2.29\mu - 120000.$
Dolomite	$k = 1.50\mu - 20000.$
Shale	$k = 1.16\mu + 10000.$
Sandstone	$k = \mu$

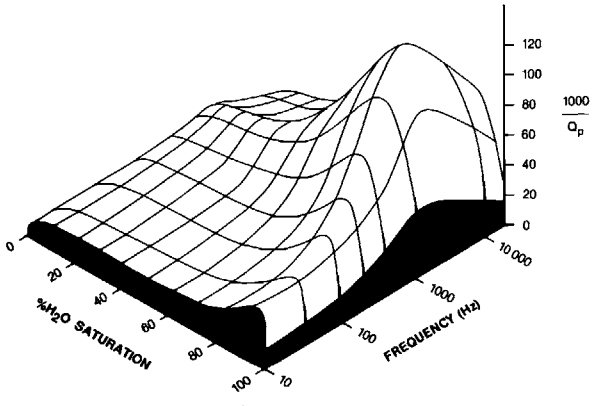

Fig. 24. Schematic representation of the dependence of compressional wave attenuation versus frequency and water-saturation (Murphy, 1982).

In reality, we expect anisotropy to be continuously frequency (and wavelength) dependent. As a convenience, however, we follow Thomsen (1986), in referring to intrinsic and extrinsic anisotropy. By intrinsic anisotropy we mean anisotropy observable on a core plug or hand specimen with dimensions on the order of a few inches. By extrinsic anisotropy we mean the difference between anisotropy observable at seismic wavelengths and ultrasonic wavelengths.

Intrinsic anisotropy may be due to preferred orientation of: (1) anisotropic mineral grains (most likely for micas and clay minerals), (2) grain shapes (such as flat-lying clay platelets of shell debris), and (3) pores or microfractures, or may be caused by fine laminations.

As a consequence of these factors, shales often have high intrinsic anisotropy. Many shales exhibit fissility as a result of preferred orientation of micas and clay minerals. Fissility decreases with increasing pressure and silica or carbonate content and increases with organic content (Pettijohn, 1975). Shales also tend to be laminated, exhibiting fine layering from .05 to 1 mm in thickness (Pettijohn, 1975). These laminations may be due to (1) alternations of silt and clay, (2) alternations of organic content, and (3) alternations of carbonate content.

Figure 26 compares *P*-wave and *S*-wave anisotropy for sandstone and shale measurements compiled in Thomsen (1986). The tendency for shales to exhibit higher anisotropy than sandstones is clear. However, some shales exhibit very low anisotropy, and there is considerable overlap with the sandstone data. Bioturbation and soft sediment deformation often destroy the initial preferred orientations and laminations in shales.

Table 13 gives bench top measurements for dry Sevier Shale samples from Tennessee. The non-fissile Rogersville sample exhibits weak compressional *P*- and *S*-wave anisotropy. In contrast, the fissile Kingsport samples exhibit extremely large anisotropy.

The effect of pressure on shale anisotropy is illustrated in Figure 27 for a well consolidated dry shale from a depth of over 19 000 ft. As pressure increases, anisotropy decreases for both *P*- and *S*-waves. The velocity increase with pressure is greatest for waves propagating perpendicular to bedding. This suggests that the anisotropy is due, in part, to preferred orientation of flat pores or cracks between clay platelets which close under pressure. The significant difference between *S*-wave velocity perpendicular to bedding and vertically polarized parallel to bedding indicates that the sample is not perfectly transversely isotropic (or perhaps not perfectly homogeneous). Similar behavior is observed for a well-consolidated, water-saturated shale from a depth of about 17 000 ft (Figure 28).

Figure 29 illustrates the behavior of an inhomogeneous water-saturated shale specimen. This specimen exhibits many features expected for transverse isotropy:

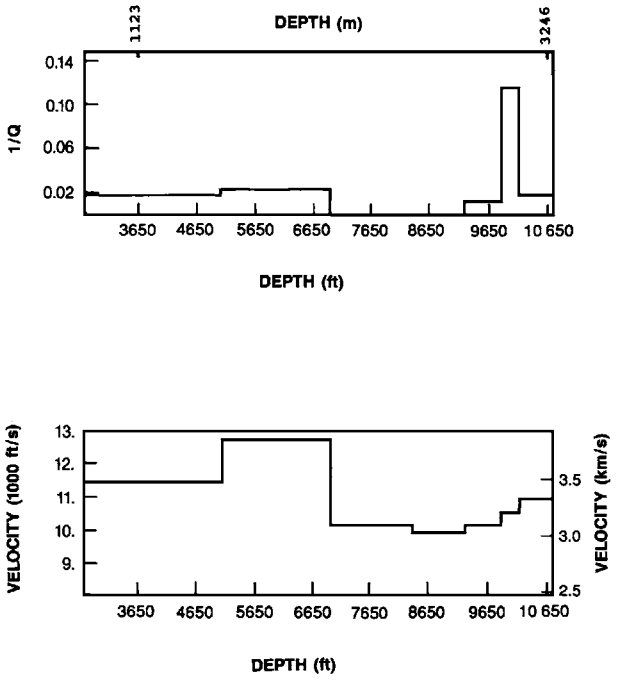

Fig. 25. Interval velocity and attenuation versus depth from a South Texas vertical seismic profile.

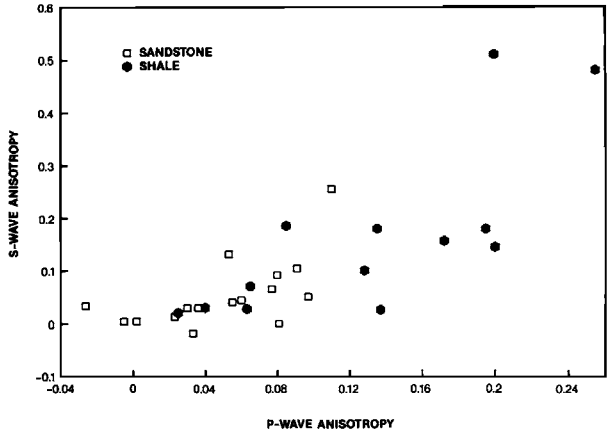

Fig. 26. *P*- and *S*-wave anisotropy for sandstones and shales for data compiled in Thomsen (1986).

Table 12. Reported in-situ attenuation measurements.

Location	Depth m	Hz	Q_p	$1/\alpha_p$	Method	Rock Type	References
Offshore Louisiana Pleistocene	2070–2850	≤125	31	.032	VSP	Sand and Clay	Hauge (1981)
Southeast Texas	660–1320	15–40	34	.027	VSP	Sand 45% and Clay	
Southeast Texas	1800–2100	≤80	37	.027	VSP	Sand 23% and Clay	
Southeast Texas	600–1560	≤80	46	.022	VSP	Sand 20% and Clay	
Offshore Louisiana Pleistocene	1170–1770	≤125	67	.015	VSP	Clay/Sand	
Southeast Texas	>1020	40–70	94	.0106	VSP	Sand 24% and Clay	
East Texas	317–402	≤200	38	.0263	VSP	Sand/Shale interbed	Kan et al (1983)
East Texas	402–610	≤200	—	$.004581f^{.35}$	VSP	Shale	
East Texas	235–371	≤200	—	$.004f^{.4}$	VSP	Shale	
East Texas	152–235	≤200	—	$.031f^{.4}$	VSP	Shale	
Beaufort Sea (Canada)	549–1193	125	43	.023	VSP		Ganley and Kanasewich (1980)
Beaufort Sea (Canada)	945–1311	425	67	.015	VSP		
Limon (Colorado)	0–225	50–450	32	.0313	VSP	Pierre Shale	McDonal et al (1958)
Gulf Coast		50–400	18	.0055	VSP	Sands and Shales	Tullos and Reid (1969)
130 km south of		50–400	75	.0133	VSP	Sandy Clay	
Houston		50–400	136	.0014	VSP	Clay/Sand	
Sarawak Basin	700	10–60	116–870		Sonobuoys	Marine Sediments	Stoll and Houtz (1983)
South China Sea	1800		137–324		Diving Wave		
San Diego	Shallow	14 KHz	31–32		Transducer	Sand	Hamilton (1972)
		14 KHz	111–437		Probes	Clay/Silt Sand/Silt/Clay	
		25 KHz	44			Fine Sand	
		25 KHz	54			Sandy Silt	
		25 KHz	118			Clayey Silt	
		100 KHz	23–104			Sand/Silt/Clay	

Table 13. Velocities parallel and orthogonal to bedding, Sevier Shale, Tennessee.

			Shear 1	Shear 2
		V_p	$Vs1$	$Vs2$
NON-FISSILE SAMPLE	⊥	5.65	3.12	3.13
(Rogersville)	∥	6.03	3.29	3.31
FISSILE SAMPLE A	⊥	1.83	—	0.61
(Kingsport)	∥	4.32	—	2.66
FISSILE SAMPLE B	⊥	1.66	0.72	0.69
(Kingsport)	∥	4.21	—	2.69

Note: V-Velocity (km/s), ⊥-Propagation perpendicular to bedding, ∥-Propagation parallel to bedding, and —Signal too poor to make determination. For propagation parallel to bedding, shear 1 is polarized with particle motion perpendicular to bedding, shear 2 is polarized with motion parallel to bedding. No confining pressure (bench-top measurements).

(1) Compressional velocity and horizontally polarized S-wave velocity parallel to bedding are greater than the compressional P- and S-wave velocities perpendicular to bedding.
(2) The anisotropy decrease with increasing pressure is due primarily to velocity increases perpendicular to bedding.
(3) For propagation perpendicular to bedding, two orthogonal polarizations of the S-wave have virtually the same velocity.

However, there is one important difference: The vertically polarized S-wave travelling parallel to bedding has about the same S-wave velocity as the horizontally-polarized S-wave travelling parallel to bedding, and has a greater velocity than the S-wave travelling perpendicular to bedding. We suspect that this is caused by layering on a scale larger than about one-tenth of an inch, which is the approximate wavelength of the ultrasonic signal. Thus, we see that at laboratory frequencies, only very fine layering can be

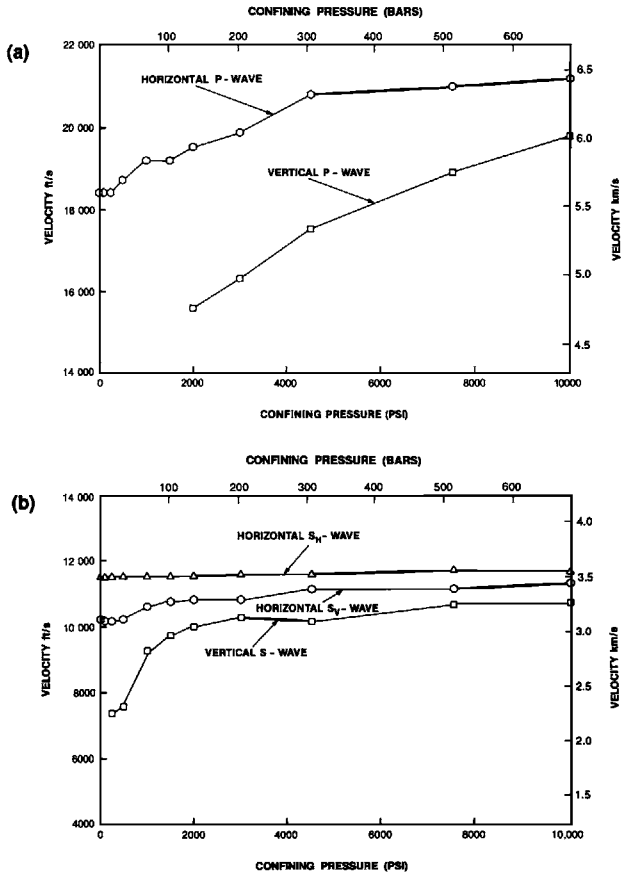

Fig. 27. Vertical and horizontal velocities versus confining pressure for a dry shale sampled from a depth of 19 454 ft (5929 m) (a) compressional velocities, (b) shear velocities.

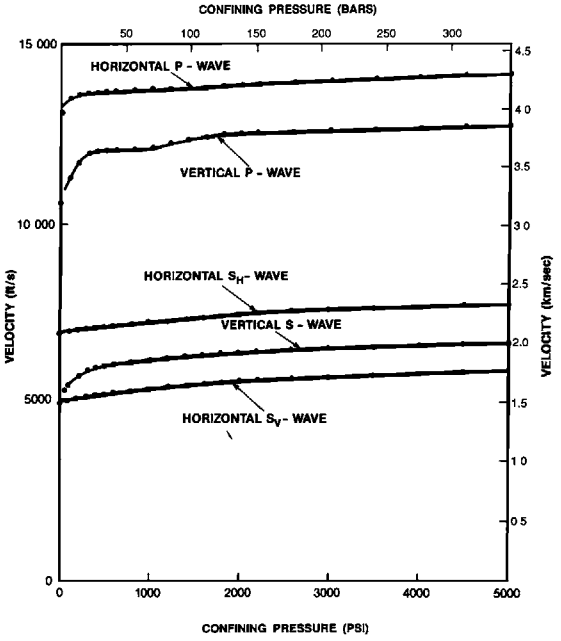

Fig. 28. Vertical and horizontal velocities for a bedded fully water-saturated shale sampled from a depth of 16 624 ft (5067 m).

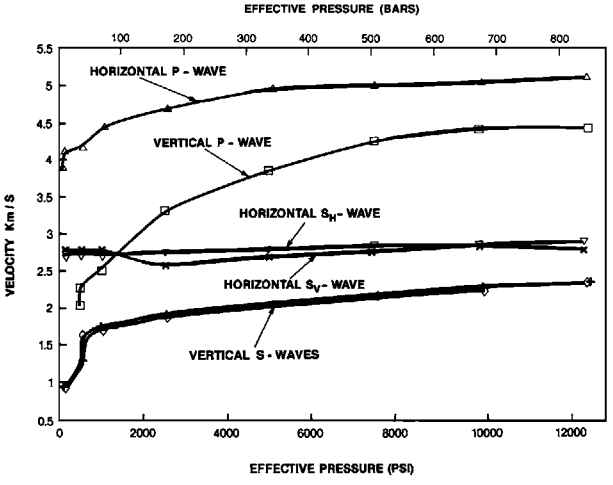

Fig. 29. Vertical and horizontal velocities for a water-saturated shale from a depth of about 17 000 ft (5181 m).

correctly characterized by bulk velocity measurements. On the other hand, we expect seismic waves to respond to anisotropy of all scales smaller than a seismic wavelength. Clearly then, laboratory measurements alone are insufficient to characterize anisotropy for seismic waves.

Extrinsic anisotropy is usually a result of geologic layering or preferred orientation of fractures. Assuming transverse isotropy, one can use the equations of Backus (1962) to average the elastic constants of layers which can be resolved by the sonic log (about 2 ft) over a seismic wavelength (hundreds of feet). Thus, given *P*- and *S*-wave velocity logs and a density log, one can compute the amount of anisotropy due to isotropic layers between 2 ft thick and some larger fraction of a seismic wavelength. We did this, choosing an arbitrary depth interval of 50 ft for each anisotropy calculation, for three different depositional settings: (1) shallow Gulf of Mexico Upper Miocene-Pliocene shales and sands, (2) shallow post-Eocene nonmarine shales and sands from the Sacramento Valley, and (3) North Slope interbedded carbonates and shales.

As shown in Table 14, for the massive Gulf of Mexico sands and shales, the mean extrinsic anisotropy is relatively small (about .5 percent for *P*-waves and 3 percent for *S*-waves). The Sacramento Valley interbedded sands and shales exhibit somewhat higher *P*- and *S*-wave anisotropy (2 and 10 percent, respectively). The interbedded North Slope carbonates and shales have the highest *P*-wave anisotropy (3 percent) but comparatively low *S*-wave anisotropy (4 percent). In the Gulf of Mexico example, calculated transverse isotropy is relatively small even though the section is predominantly shale because the shales and sands are massive and have a low degree of interbedding. In the Sacramento Valley example, there is a great deal of sand-shale interbedding and anisotropy is high. *S*-wave anisotropy is much greater than *P*-wave anisotropy because V_p/V_s is strongly correlated to *P*-wave slowness. In contrast, the interbedded North Slope shales and carbonates exhibit relatively high *P*-wave anisotropy due to the strong *P*-wave velocity contrasts, but only slightly greater *S*-wave anisotropy due to the relatively constant V_p/V_s ratios of the shales and carbonates.

It should be emphasized that these calculations predict only anisotropy induced by layers which can be resolved by the sonic log. Additional anisotropy can be expected from finer layers and intrinsic anisotropy. However, some conclusions of consequence can be drawn from these calculations: (1) The magnitudes of the predicted anisotropies in Table 14 are about the same as observed intrinsic anisotropies. Thus, we conclude that transverse layering can be as important as intrinsic anisotropy. (2) The degree of anisotropy is strongly dependent on the amount of interbedding and consequently the depositional environment. Knowledge of depositional environment may allow estimation of anisotropy which can be input into elastic modeling algorithms to aid AVO analysis. Conversely, anisotropy estimates extracted from the seismic data may be useful facies indicators. (3) Although the amount of anisotropy may not be easily related to lithology, comparing *P*- and *S*-wave anisotropy may provide some insight into the mix of lithologies. We have seen that interbedded isotropic sandstones and shales tend to have much higher *S*-wave anisotropy relative to the *P*-wave while interbedded isotropic carbonates and shales of similar V_p/V_s ratio have similar *P*- and *S*-wave anisotropy.

In practice, anisotropy is not necessarily transverse. Azimuthal anisotropy can be developed when there is structural complexity or the rocks are fractured. Numerous theories exist to calculate the effects of a population of oriented fractures with specified characteristics. Unfortunately, as with the geometry specific poroelastic models, information is required about the fracture shapes, densities, etc. Solutions are not unique, so measured anisotropy cannot unambiguously be related to the fracture characteristics. However, oriented microfractures have been demonstrated

Table 14. Calculated transverse anisotropy from compressional and shear wave velocity and density logs for 15 m thick intervals using the Backus (1962) elastic moduli averaging equations.

Area	Depth Range	Lithology	Parameter	Min	Max	Mean	Std. Dev
Gulf of Mexico	1025′–3775′	sh and ss	E	−.024	.021	.005	.005
			G	.001	.156	.032	.029
Sacramento Valley	1525′–3000′	sh and ss	E	.001	.161	.023	.024
			G	.003	.502	.103	.077
North Slope	8805′–10 075′	lms and sh	E	.000	.115	.030	.026
			G	.002	.165	.041	.037

Note: E = compressional-wave anisotropy, G = shear-wave anisotropy

to have a substantial effect on ultrasonic velocities. For example, by applying a uniaxial stress we would expect to open fractures parallel to this stress. Hence, velocities should increase for propagations parallel to the stress and decrease normal to the stress. This effect has been reported in Volarovich et al. (1985). Alternatively, Engelder and Plumb (1984) attributed the measured azimuthal velocity anisotropy of core samples to microfractures opening from stress relief caused by the coring process.

CONCLUSIONS

Various key rock physics issues are directly relevant to amplitude variation with offset analysis. These include V_p-V_s, V_p-density, and velocity-lithology-porosity relations, pore fluid properties, fluid substitution, skeleton properties, attenuation, and anisotropy. We find that:

(1) V_p-V_s relationships are simply related to lithology and pore fluid content,
(2) Velocity-density relationships are highly variable,
(3) Pore fluid properties are highly variable and vary systematically,
(4) Skeleton moduli trends can be derived from water-saturated measurements,
(5) Gas-bearing rocks exhibit anomalously high attenuation, and
(6) Anisotropy due to transverse layering can be as important as intrinsic anisotropy.

These conclusions provide a framework for the interpretation of amplitude variation with offset data.

ACKNOWLEDGMENTS

Thanks to ARCO Oil and Gas Company for permission to publish this paper. Special thanks to M. Popa, B. Smith, C. Landisman and M. Backus for their contributions. If not for S. Gronemeier, this paper would never have been completed.

APPENDIX A—MORE PRESSURE CONCEPTS

Pressure is defined as normal force per unit area. Table A-1 provides conversion factors between various units of pressure. Overburden pressure (P_o) is the pressure due to the weight of fluid-saturated rock and is given by

$$P_o(z) = \bar{\rho}_b(z)gh = g\int_0^h \rho_b(z)\,dz \qquad \text{(A-1)}$$

where

$\bar{\rho}_b(z)$ = mean overburden fluid-saturated bulk density as a function of depth,
g = acceleration due to gravity,
h = total depth,
z = depth, and
$\rho_b(z)$ = fluid-saturated bulk density as a function of depth.

Similarly, hydrostatic pressure (P_h) is the pressure due to the weight of a column of fluid, and is given by:

$$P_h(z) = \bar{\rho}_f(z)gh = g\int_0^h \rho_f(z)\,dz \qquad \text{(A-2)}$$

where

$\bar{\rho}_f(z)$ = mean overburden pore-fluid density as a function of depth, and
$\rho_f(z)$ = pore fluid density as a function of depth.

In engineering practice, pressure gradients are defined as pressure divided by depth, rather than, dP/dz, which is the "true" pressure gradient. Thus, the overburden pressure gradient is P_o/z and the hydrostatic pressure gradient is P_h/z. Various pressure gradient units are given in Table A-2.

Table A-1. Conversion table for units of pressure (after Billings; 1972).

Pounds per Square Inch	Atmospheres	Bars	Mega Pascals (MPa)
1	0.0680458	0.0689474	.0069
14.6960	1	1.01325	.1013
14.5038	0.986924	1	.1
14.2234	0.967842	0.980665	.0981
.000014504	.000000986924	.000001	.0000001
145.038	9.86924	.10	.01

Table A-2. Densities and associated pressure gradients (after Gretener, 1979).

Oil: g/cc	API° (60°F)	psi/ft	MPa/ft	MPa/m	bars/m	bars/ft
0.7	70.6	0.303	.00209	0.0069	.069	.0209
0.8	45.4	0.346	.00239	0.0078	.078	.0239
0.9	25.7	0.390	.00269	0.0088	.088	.0269
1.0	10.0	0.433	.00299	0.0098	.098	.0299
Formation Waters:						
g/cc	total solids ppm	psi/ft	MPa/ft	MPa/m	bars/m	bars/ft
	0	0.433	.00299	0.0098	.098	.0209
1.00	28,000	0.441	.00305	0.0100	.100	.0305
1.02	55,000	0.450	.0031	0.0102	.102	.0311
1.04	84,000	0.459	.00317	0.0104	.104	.0317
1.06	113,000	0.467	.00323	0.0106	.106	.0323
1.08	144,000	0.476	.00329	0.0108	.108	.0329
1.10	176,000	0.485	.00335	0.0110	.110	.0335
1.12	210,000	0.493	.00341	0.0112	.112	.0341
sea water:						
1.025	35,000	0.443		0.0100	.100	

Rocks, Drilling Mud: g/cc	Lb/ft^3	Lb/gal	psi/ft	MPa/ft	MPa/m	bars/m	bars/ft
1.0	62.4	8.35	0.433	.00299	0.0098	.098	.0299
1.2	74.9	10.02	0.520	.00359	0.0118	.118	.0359
1.4	87.4	11.69	0.607	.00419	0.0137	.137	.0419
1.6	99.8	13.36	0.693	.00478	0.0157	.157	.0478
1.8	112.3	15.03	0.780	.00538	0.0176	.176	.0538
2.0	124.8	16.70	0.867	.00598	0.0196	.196	.0598
2.2	137.3	18.37	0.953	.00658	0.0216	.216	.0658
2.4	149.8	20.04	1.040	.00718	0.0235	.235	.0718
2.6	162.2	21.71	1.126	.00777	0.0255	.255	.0777
2.8	174.7	23.38	1.213	.00837	0.0274	.274	.0837
3.0	187.2	25.05	1.300	.00897	0.0294	.294	.0897

*Strictly speaking, pressure gradients are related to the specific weight (γ) rather than the density (ρ). Note: $\gamma = \rho * g$, where g: 980.665 cm/s^2.

Table A-3. Example density-depth functions for various sedimentary sections world-wide. Functions may be for specific locations and are not necessarily statistically representative for a wide geographic area. Curve letters refer to Figure A-1. ρ_b = bulk rock density. z = depth.

	Curve area	Equation	Remarks
A	Kentucky	$\rho_b = 2.76 + .059z + .026z^2$	Borehole gravity; Chapin (ARCO data)
B	Michigan	$\rho_b = 2.63 + .049z$	Borehole gravity; Chapin (ARCO data)
C	Delaware Basin	$\rho_b = 2.52 + .029z$	Gravity model; Keller et al. (1985)
D	Western Ross Sea	$\rho_b = 2.00 + .254z - .021z^2$	Gravity model; Davey and Cooper (1987)
E	Santa Barbara Channel	$\rho_b = 2.05 + .160z - .020z^2$	Well data; Fertl (1976)
F	Deep Sea Terrigenous Sediments	$\rho_b = 1.53 + 1.39z - .617z^2$	Core; Hamilton (1976)
G	Gulf Coast Shales	$\rho_b = 2.14 + .505 \log z$	Well data; Dickinson (1953)
H	Offshore Morocco	$\rho_b = 1.75 + .200z - .010z^2$	Gravity model; Hinz et al. (1982)
I	Ventura Basin	$\rho_b = 2.19 + .035z$	Gravity model; Jachens and Griscom (1985)
J	North Sea	$\rho_b = 1.98 + .118z - .012z^2$	Well data; Fertl (1976)
K	Gulf Coast	$\rho_b = 1.95 + .108z - .009z^2$	Well data; Fertl (1976)

Figure A-1 shows typical average overburden density functions, $\bar{\rho}_b(z)$, and associated pressure gradients for various locations worldwide. The average density functions were obtained by integrating the density-depth functions given in Table A-3.

Figure A-2 shows overburden pressure gradients versus depth as a function of age used by drilling engineers for fracturing/completions calculations. As expected, older rocks tend to exhibit higher overburden pressure gradients.

Inspection of Figures A-1 and A-2 reveals that the common assumption that overburden pressure gradients are "about 1 psi/ft" can be grossly in error, particularly for young unconsolidated clastics and predominantly carbonate or Paleozoic age geologic columns.

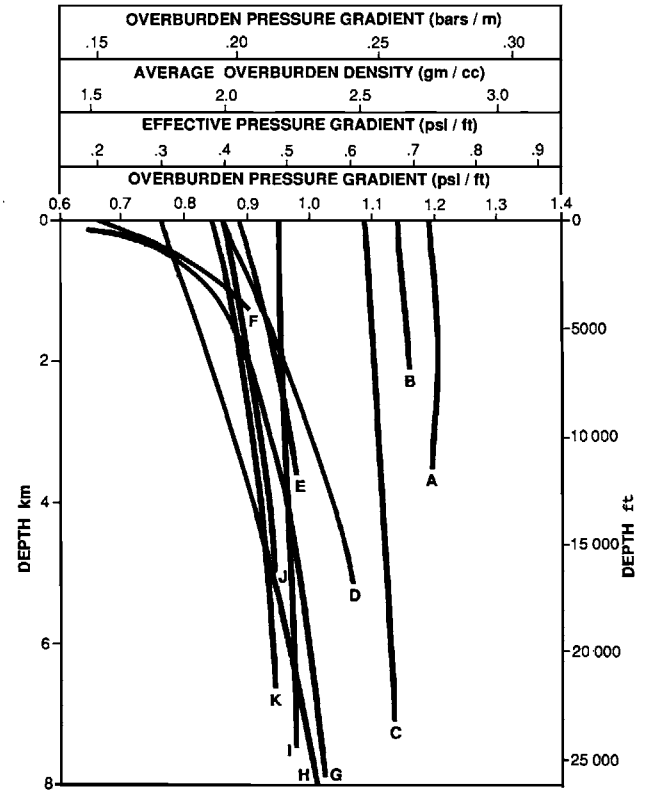

Fig. A-1. Overburden pressure gradients for various localities world-wide. See Table A-3 for locations, associated density-depth functions, and sources of data.

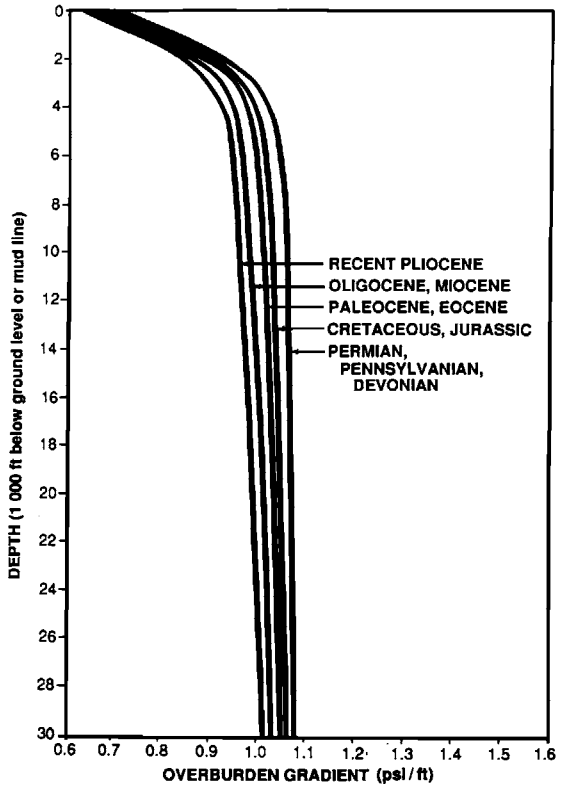

Fig. A-2. Overburden pressure gradients commonly used by engineers (from Matthews and Matthews; 1985).

APPENDIX B—COMPRESSIONAL- AND SHEAR-WAVE VELOCITY IN COAL

We can report only limited reliable S-wave velocity information for coals.

Table B-1 gives velocities of Permian bituminous coals from the Sydney Basin, New South Wales, presented by Greenhalgh and Emerson at the 1981 SEG Convention.

Figure B-1 shows velocity measurements on two samples of Ferron coal under wet and dry saturation conditions and for effective stresses from 34 to 1034 bars. There is no significant difference in the V_p-V_s trends of the dry and water-saturated data.

Figure B-2 combines the data from Table B-1 and Figure B-1 and shows the resulting second-order polynomial fit. Table B-2 gives the regression coefficients. The reader is cautioned that this trend is for a very limited dataset and that further data are required to establish a more universally applicable

Table B-1. Physical properties of Permian bituminous coals from the Sydney Basin, New South Wales (Greenhalgh and Emerson, 1981). Pressure and saturation conditions for velocity measurements were unspecified. Dry bulk densities: 1.34 to 1.45 gm/cc. Effective porosity: 1 to 9 percent, mean 4 percent.

Propagation direction	Mean V_p (km/s)	Mean V_s (km/s)	V_p/V_s
Perpendicular to bedding	≈2.0	.96	2.08
Parallel to bedding	≈2.3	1.08	2.13
Perpendicular to bedding	1.74	≈.8	2.18
Parallel to bedding	1.85	≈.8	2.31

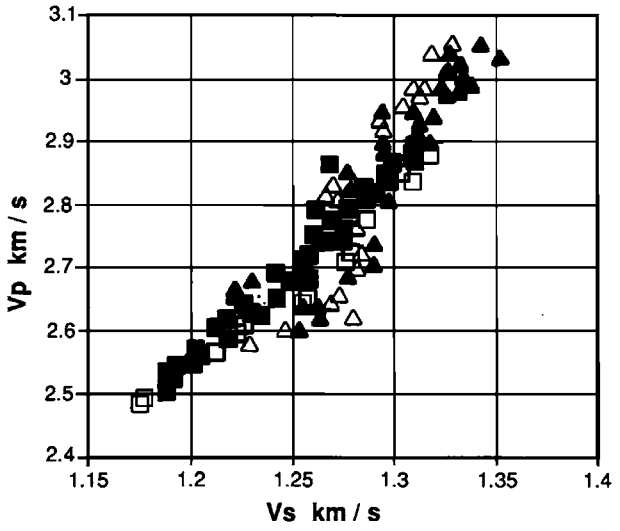

Fig. B-1. Velocity measurements on two samples of Ferron coal for effective stresses from 34 to 1034 bars. Solid symbols are fully water-saturated measurements. Open symbols are dry.

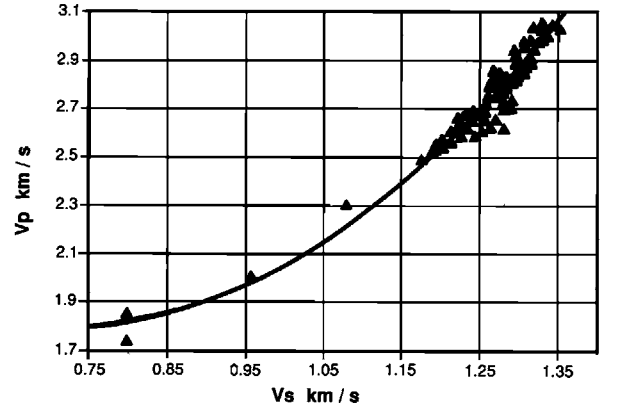

Fig. B-2. V_p-V_s relationship for coal combining data from Table B-1 and Figure B-1.

Table B-2. Regression coefficients for coal V_p-V_s trend (for velocity units of km/s).

(a) $V_p = aV_s^2 + bV_s + c$

Coefficient	Value	Standard Error
a	3.162	.296
b	−4.535	.664
c	3.420	.052
R-squared	.934	
Observations	143	

(b) $V_s = dV_p^2 + eV_p + f$

Coefficient	Value	Standard Error
d	−0.232	.012
e	1.542	.064
f	−1.214	.014
R-squared	.966	
Observations	143	

V_p-V_s relationship. In particular, the variation of V_p-V_s relationship with coal grade has yet to be reported.

APPENDIX C—EFFECT OF DISSOLVED GAS ON WATER MODULUS

Equation (48) provides the relationship between isothermal water modulus and gas-water ratio. For velocity calculations, the adiabatic modulus is required. If we assume equation (48) to hold for adiabatic conditions, we can calculate fluid modulus versus temperature, pressure, and gas-water ratio. Plots

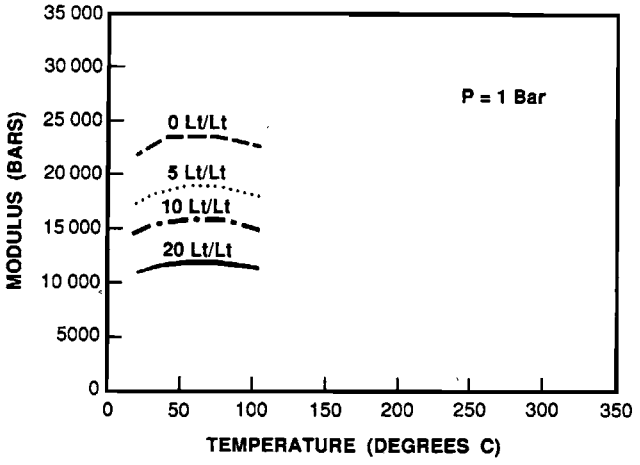

Fig. C-1. Tenuous water modulus versus temperature and gas-water ratio at a pressure of 1 bar.

of these calculations are provided as Appendix C rather than in the main body of this paper due to (1) the inadequate documentation provided in Dodson and Shanding (1948) regarding the empirical determination of equation (48) and, (2) the assumption that equation (48) does indeed apply for the adiabatic modulus. Thus, the modulus plots provided here (Figures C-1 through C-3) must be considered highly tenuous and subject to change as more data become available. Figures C-1 through C-3 have been included primarily to emphasize the importance of dissolved gas on water modulus, to illustrate the systematics of modulus variation, and to provide a rough estimate of the modulus only when better information is lacking.

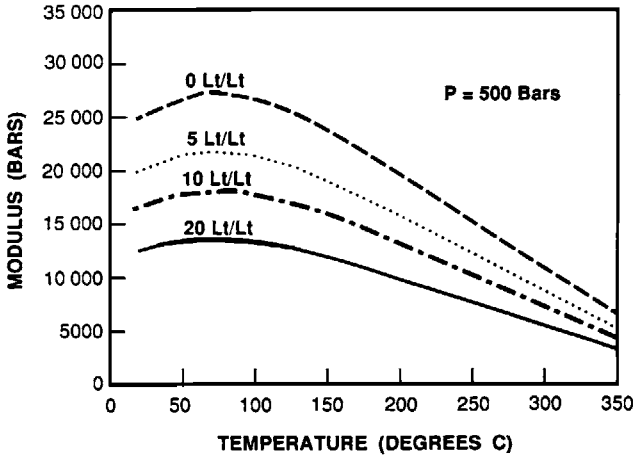

Fig. C-2. Tenuous water modulus versus temperature and gas-water ratio at a pressure of 500 bars.

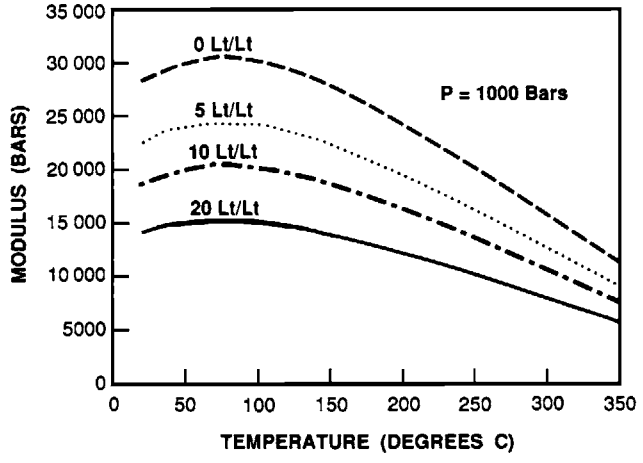

Fig. C-3. Tenuous water modulus versus temperature and gas-water ratio at a pressure of 1000 bars.

APPENDIX D—PROPERTIES OF SHALES

Although shale is the most abundant sedimentary rock component of the stratigraphic column worldwide, it is also the most poorly understood of the common sedimentary rocks. The physical, chemical, transport, electrical, and acoustic properties of shales are not well established. Even a definition of what constitutes a shale is generally unavailable. From the perspective of seismic explorationists, a knowledge of shale physical and acoustic properties is needed to interpret reflection amplitudes and to understand transmission effects above the target.

Rock physicists are faced with a number of difficult challenges when attempting to study shale properties:

(1) It is generally very difficult to obtain unaltered shale core samples and to perform velocity and physical properties measurements on them under in situ conditions. This is also compounded by the difficulty in economically justifying the costs of coring and analysis for nonreservoir rocks.
(2) Mineralogical analysis is greatly hindered by the extremely fine grain size of the clay particles. Mineral abundances can only be roughly estimated by painstaking X-ray diffraction analysis or by attempting to unravel bulk chemical and physical property analyses. This becomes very important in the study of diagenetic alteration which is required for an understanding of depth-dependent variations.
(3) Many shale properties are interrelated and it is often difficult to isolate them. For example, the relationship between velocity and effective stress may be difficult to separate from the relationship between porosity and effective stress.

While compiling data for shales, we came across three sources: (1) compaction measurements carried out on natural sediments and clay slurries, (2) in situ measurements based on wireline logs, and (3) laboratory measurements on core samples restored to in situ conditions. While laboratory measurements on clay-rich rocks are valuable, laboratory derived velocity-pressure curves may be questionable due to problems in achieving pore pressure equilibrium within the limited time available for laboratory measurements. Shales are known to exhibit long term "creep" phenomenon and, therefore, most of the data in the literature from such measurements must be inter-

Table D-1. Shale terminology.

Term	Definition
Silt	Particle between 1/16 and 1/256 of an inch in diameter.
Clay	Particle smaller than 1/256 of an inch.
Clay Minerals	A group of hydrous aluminum silicates exhibiting a sheet-like structure similar to mica. Clays usually result from the weathering of feldspars. For our purposes, we will also consider micas as clay minerals.
Mud	Silt and clay.
Mudrock	Lithified mud.
Fissility	The tendency of a rock to separate along smooth surfaces parallel to bedding.
Siltstone	A non-fissile mudrock composed of two-thirds silt or more.
Claystone	A non-fissile mudrock composed of two-thirds clay or more.
Shale (strict definition)	A fissile mudrock.
Shale (general usage)	A mudrock rich in clay minerals.

preted with caution. Notably, Johnston (1986) paid special attention to ensuring that his samples had sufficient time to equilibrate. Wireline measurements are valuable in establishing shale properties versus depth in a given area, but suffer from borehole alteration. They are also restrictive in that there are no means for controlling the independent variables such as effective stress.

Terminology for fine-grained clastic silicate rocks is not well established. We follow the terminology of Blatt et al. (1972) given in Table D-1. We use the term "shale" in the most general sense. It is common in logging to define "clean shales" based solely on the SP or gamma ray response. Hence, rocks often referred to as shales can actually be a host of materials.

Table D-2. Some reported mineral compositions of shales (percent).

Paleozoic and younger shales: Shaw and Weaver (1965)		
Constituent	Range	Mean
Clay minerals	<20–90	61
Quartz	10–80	31
Feldspar	0–30	4.5
Carbonates		3.6
Iron oxides		<0.5
Miscellaneous		<2
Organic matter		1

Calcareous Devonian shales of Alberta: Campbell and Oliver (1968)	
Constituent	Range
Illite	13–39
Quartz	3–26
Dolomite	1–36
Calcite	16–76

Shales are mixtures of clay-sized particles, consisting primarily of clay minerals, and silt particles, which are mostly quartz. Krynine (1948) estimated the "average" shale to be about 50 percent silt, while Pettijohn (1975) and others suggest that shales average about two-thirds silt. Mineralogically, shales tend to be composed of about half clay minerals; the rest being primarily quartz plus a few percent feldspar and calcite. Table D-2 shows shale compositions reported in Shaw and Weaver (1965) for 300 samples of Paleozoic and younger shales and by Campbell and Oliver (1968) for calcareous Devonian shales in Alberta. Note that quartz content can be as great as 80 percent, that clay content can be less than 20 percent, and that carbonate content forms a continuum between shale and limestone.

Figure D-1 from Pettijohn (1975) shows the structure of clay minerals. The basic building blocks of clay minerals are (a) silica tetrahedral layers, (b) aluminum and/or magnesium hydroxide octahedral layers, and (c) interlayer water molecules and cations. The simplest clay structure is that of kaolinite, which is essentially a stack of two-layer units, each containing one octahedral and one tetrahedral layer. Montmorillonite consists of three-layer units, each containing one octahedral and two tetrahedral layers. The units are bound to each other by water molecules and cations such as sodium, potassium, magnesium, and calcium. The number of water molecules is governed by volumetrics, rather than stochiometry, and the structure can expand to accommodate more water. The mica, muscovite, is also composed of three-layer units, however, the units are held together exclusively by potassium cations and there is substitution of aluminum for silicon in the tetrahedral layers. Illite is

essentially hydrous muscovite, with a combination of water molecules and potassium cations bonding the three-layer units and less aluminum for silicon substitution. Chlorite consists of three-layer units bonded to each other by single magnesium hydroxide octahedral layers. Mixed-layer clays are stacks of alternating clay types such as kaolinite-illite or montmorillonite-illite. The alternations may be random or may have varying degrees of order. Cation substitution is common in clay minerals, so compositions generally vary greatly.

The distribution of clay minerals encountered in a sedimentary section depends on a number of factors including (a) source, (b) paleoclimate, (c) hydraulic sorting, and (d) diagenesis. Factors such as the chemical environment of deposition are believed to be of lesser importance. When shale/clay composition is plotted versus time (see Figure D-2) there is a clear tendency for an increase in chlorite and illite content at the expense of other clays with increasing age. This is presumably primarily a diagenetic effect. The irregularity of the curves can be explained by variations with time in factors (a) thru (c) presented earlier and variations in factors affecting diagenesis, such as geothermal gradient.

Upon deposition, clay sediment porosities may be as high as 90 percent. As a result of compaction, porosities decrease rapidly with depth. According to Rieke and Chilingarian (1974), shale porosity at 5000 ft varies from about 5 percent to 25 percent (see Figure D-3). Hedburg (1936) gives 9 percent as average shale porosity at 6000 ft, although density log readings indicate that shales typically have much larger water contents by volume at this depth. The primary factor controlling shale porosity is effective stress, but infilling of pores by diagenesis is also important (Pettijohn, 1975). Judd and Shakoor (1981) report shale densities from .97 (loose clays) to 2.72 gm/cc with a mean of 2.34 and a standard deviation of .379.

As described in the main body of this paper, velocity-density relationships may be quite variable for shales. Figure D-4 shows velocity-density data for shales from the DOE Pleasant Bayou #1 and #2 wells in Brazoria Co., Texas. There are two distinct groups of data corresponding to shales shallower than 8000 ft. and deeper than 12 000 ft. Note that these groups fall below the Gardner curve and exhibit two distinctly different velocity-density trends. This change in be-

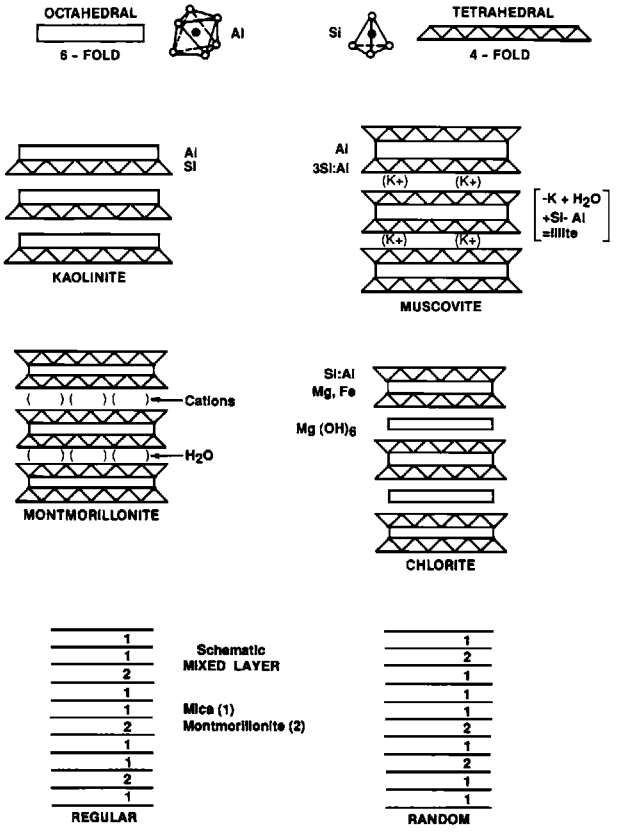

Fig. D-1. Structure of clay minerals from Pettijohn (1975).

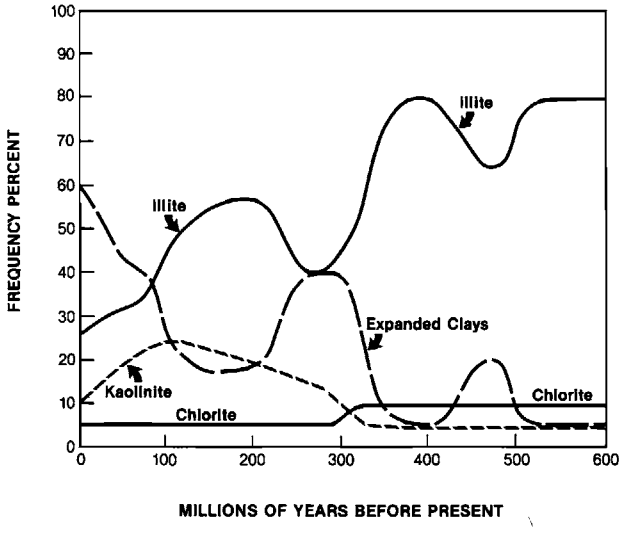

Fig. D-2. Shale clay composition as a function of geologic time from Blatt et al. (1972).

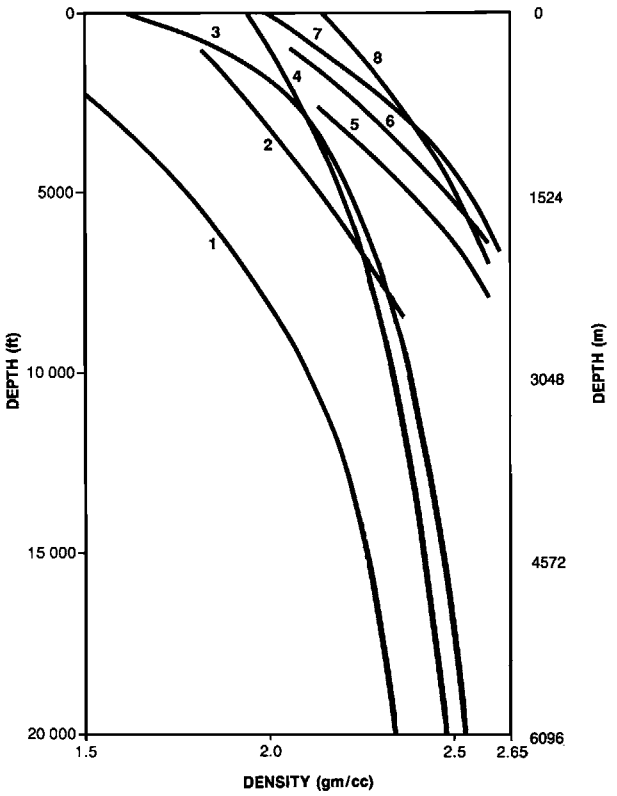

Fig. D-3. Variation of shale bulk densities with depth in sedimentary basins. 1 = methane-saturated clastic sedimentary rock (probable minimum density) (after McCulloh, 1967, p. A19); 2 = mudstone-Po Valley Basin, Italy, (after Storer, 1959); 3 = average Gulf Coast shale densities; values derived from geophysical data (after Dickinson, 1953, p. 427); 4 = average Gulf Coast shale densities derived from density logs and formation samples (after Eaton, 1969); 5 = Motatan-1-Maracaibo Basin, Venezuela (after Dallmus, 1958, p. 916); 6 = Gorgeteb No. 1—Hungary; calculated wet density values (after Skeels, 1943, unpublished material); 7 = Pennsylvanian and Permian dry shale density values, Oklahoma and Texas; Athy's adjusted curve (after Dallmus, 1958, p. 913); 8 = Las Ollas-1-eastern Venezuela (after Dallmus, 1958, p. 918). From Rieke and Chillingarian (1974).

havior is associated with the montmorillonite-illite transition which occurs at about 10 000 ft. The change in velocity-density behavior may be due directly to this change in mineralogy and/or may be associated with geopressuring.

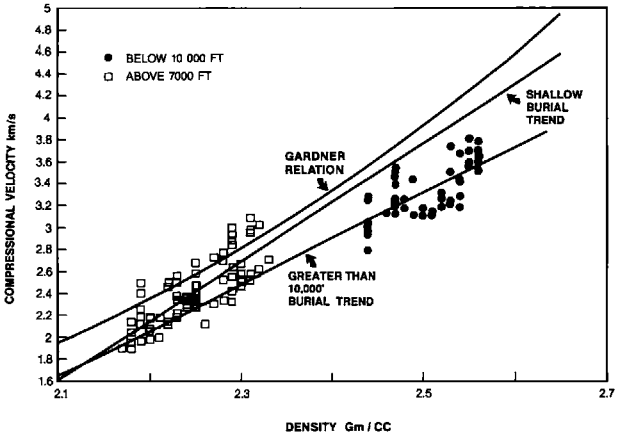

Fig. D-4. Velocity-density crossplot for shales from DOE Pleasant Bayou #1 and #2 wells in Brazoria, Co., Texas.

APPENDIX E—ROUGH APPROXIMATION RELATING GAS SAND AND BRINE SAND VELOCITIES

By assuming equality of sandstone frame bulk and shear moduli, Gassmann's equations may be used to compute gas sand compressional velocity as a function of fully saturated water sand velocity if the skeleton properties are assumed to be unchanged by the pore fluid. If the modified Gardner equation is used to estimate porosity, skeleton bulk modulus and shear modulus are assumed to be equal (Castagna, et al. 1985), and water saturation is taken to be 50 percent, gas sand compressional velocity (V_{pgas}) as given by (see Figure E-1):

$$V_{\text{pgas}} = .07V_p^2 + 1.67V_p - 1.74$$

where V_p = brine-saturated compressional velocity.

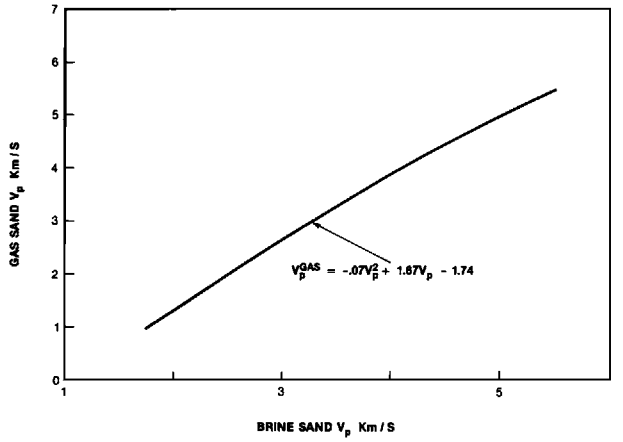

Fig. E-1. Rough relationship between brine-sand and gas-sand velocity using assumptions described in text.

REFERENCES

Aleksandrov, K. S., and Ryzhova, T. V., 1961, The elastic properties of crystals: Sov. Phys. Crystallgr., **6**, 228.

Anderson, O. L., and Lieberman, R. C., 1966, Sound velocities in rocks and minerals: VESIAC state-of-the-art report no. 7885-4-X Univ. of Michigan.

Anderson, R. G., and Castagna, J. P., 1984, Analysis of sonic log compressional wave amplitudes using borehole compensation techniques: Soc. Prof. Well Log Analysts 25th Annual Symposium, Transactions, paper K.

Backus, G. E., 1962, Long-wave elastic anisotropy produced by horizontal layering: J. Geophys. Res., **67**, 4427–4440.

Batzle, M. L., and Wang, Z. J., 1992, Seismic properties of pore fluids: Geophysics, **57**, 1396–1408.

Billings, M. P., 1972, Structural geology: Prentice-Hall.

Biot, M. A., 1956, The theory of propagation of elastic waves in a fluid-saturated solid, I lower frequency range, II higher frequency range: J. Acoust. Soc. Am., **28**, 179–191.

Biot, M. A., 1962, Mechanics of deformation and acoustic propagation in porous media: J. Appl. Phys., **23**, 1482–1498.

Birch, F., 1966, Compressibility; elastic constants, Clark, S. P., Jr., Ed., *in* Handbook of physical constants: Geol. Soc. Am., Memoir, **97**, 97–174.

Blatt, H., Middleton, G. V., and Murray, R. C., 1972, Origin of sedimentary rocks: Prentice-Hall.

Brill, J. P., and Beggs, H. D., 1977, Two phase flow in pipes: University of Tulsa.

Bulau, J. R., Tittman, B. R., Abdel-Gawad, M., and Salvado, D., 1984, The role of aqueous fluids in the internal friction of rock: J. Geophys. Res., **89**, 4207–4212.

Campbell, F. A., and Oliver, T. A., 1968, Mineralogic and chemical composition of Freton and Duvernay Formations Central Alberta: Bull. Canadian Pet. Geol., **16**, 40–63.

Castagna, J. P., Batzle, M. L., and Eastwood, R. L., 1985, Relationships between compressional-wave and shear-wave velocities in clastic silicate rocks: Geophysics, **50**, 571–581.

Castagna, J. P., 1985, Shear-wave time-average equation for sandstones: Presented at the 55th Ann. Internat. Mtg., Soc. Expl. Geophys.

Chen, C. T., Chen, L. S., and Millero, F. J., 1978, Speed of sound in NaCl, $MgCl_2$, Na_2So4, and $MgSO_4$ aqueous solutions as functions of concentration, temperature, and pressure: J. Acoust. Soc. Am., **63**, 1795–1800.

Culberson, O. L., and McKetta, J. J., Jr., 1951, The Solubility of methane in water at pressures to 10,000 PSIA: Petroleum Trans., AIME, **192**, 223–226.

Dallmus, K. F., 1958, Mechanics of basin evolution and its relation to the habitat of oil in the basin, *in* Weeks, L. G., Ed., Habitat of oil: Am. Assoc. Pet. Geologists, Mem. **36**, 2071–2174.

Dandekar, D. P., 1968, Pressure dependence of the elastic constants of calcite: Phys. Rev., **172**, 873.

Davey, F. J., and Cooper, A. K., 1987, Gravity studies of the Victoria Land Basin and Iselin Bank, *in* Cooper, A. K., and Davey, F. J., Eds., the Antarctic Continental Margin and Geophysics of the Western Ross Sea, CPCEMR Earth Science Series, V. J. B., Houston, Texas: Circum-Pacific Council for Energy and Mineral Resources.

DeVilbiss, J., Ito, H., and Nur, A., 1979, Measurement of compressional and shear wave velocities of water filled rocks during water-steam transition: Geophysics, **44**, 407.

Dickinson, G., 1953, Geological aspects of abnormal reservoir pressures in Gulf Coast Louisiana: Am. Assn. Petr. Geol., **37**, 410–432.

Dickey, P. A., 1966, Patterns of chemical composition in deep subsurface waters: Am. Assn. Petr. Geol., **50**, 2472–2478.

Dodson, C. R., and Standing, M. B., 1945, Pressure-volume-temperature and solubility relations for natural-gas-water mixtures, *in* Drilling and production practices, 1944: Am. Pet. Inst., 173–179.

Domenico, S. N., 1976, Effect of brine-gas mixture on velocity in an unconsolidated sand reservoir: Geophysics, **41**, 887–894.

Domenico, S. N., 1977, Elastic properties of unconsolidated porous sand reservoirs: Geophysics, **42**, 1339–1369.

Domenico, S. N., 1984, Rock lithology and porosity determination from shear and compressional wave velocity: Geophysics, **49**, 1188–1195.

Eastwood, R. L., and Castagna, J. P., 1986, Interpretation of V_p/V_s ratios from sonic logs, *in* Danbom, S. H., and Domenico, S. N., Eds., Shear wave exploration, Geophysical Developments No. 1: Soc. of Expl. Geophys.

Eaton, B. A., 1969, Fracture gradient prediction and its application to oil-field operations: J. Pet. Tech., **21**, 1353–1360.

Eberhart-Phillips, D., Han, D. H., and Zoback, M. D., 1989, Empirical relationships among seismic velocity, effective pressure, porosity, and clay content in sandstone: Geophysics, **54**, 82–89.

Engelder, T., and Plumb, R., 1984, The relation between ultrasonic properties and strain relaxation: Int. J. Rock Mech., Min. Sci. and Geomech. Abs., **21**, 74–83.

Fertl, W. H., 1976, Abnormal formation pressures: Elsevier.

Freed, R. L., 1980, Shale mineralogy of the No. 1 Pleasant Bayou Geothermal Test Well, a progress report, *in* Proceedings 4th United States Gulf Coast Geopressured-Geothermal Energy Conference, Research and Development, V.1: Center for Energy Studies, University of Texas—Austin.

Ganley, D. C., Kanasewich, E. R., 1980, Measurement of absorption and dispersion from check shot surveys: J. Geophys. Res., **85**, 5219–5226.

Gardner, G. H. F., Gardner, L. W., and Gregory, A. R., 1974, Formation velocity and density—The diagnostic basis for stratigraphic traps: Geophysics, **39**, 770–780.

Gassman, F., 1951, Elastic waves through a packing of spheres: Geophysics, **16**, 673–685.

Greenhalgh, S. A., and Emerson, D. W., 1981, Physical properties of Permian bituminous coals from the Sydney Basin, New South Wales: Presented at the 51st Ann. Internat. Mtg., Soc. Expl. Geophys.

Gregory, A. R., 1976, Fluid saturation effects on dynamic elastic properties of sedimentary rocks: Geophysics, **41**, 895–921.

Gregory, A. R., 1977, Aspects of rock physics from laboratory and log data that are important to seismic interpretation, *in* Seismic stratigraphy—Application to hydrocarbon exploration: Memoir 26, Am. Assn. Petr. Geol.

Gretener, P. E., 1979, Pore pressure: fundamentals, general ramifications, and implications for structural geology (revised): Education Course Notes Series No. 4, Am. Assn. Petr. Geol.

Gretener, P. E., 1981, Geothermics—using temperature in hydrocarbon exploration: Education Course Notes Series No. 17, Am. Assn. Petr. Geol.

Hadley, K., 1976, Comparison of calculated and observed crack densities and seismic velocities in Westerly Granite: J. Geophys. Res., **81**, 3484–3494.
Hamilton, E. L., 1972, Compressional-wave attenuation in marine sediments: Geophysics, **37**, 620–646.
Hamilton, E. L., 1976, Variations of density and porosity with depth in deep-sea sediments: Jour. Sed. Pet., **46**, 280–300.
Han, De-hua, Nur, A., and Morgan, D., 1986, Effects of porosity and clay content on wave velocities in sandstones: Geophysics, **51**, 2093–2107.
Hauge, P. S., 1981, Measurement of attenuation from vertical seismic profiles: Geophysics, **46**, 1548–1558.
Hedburg, H. D., 1936, Gravitational compaction of clays and shales: Am. J. Sci., **31**, 241–281.
Hegelson, H. C., and Kirkham, D. H., 1974, Theoretical prediction of the thermodynamic behavior of aqueous electrolytes: Am. J. Sci., **274**, 1089–1198.
Hill, R., 1952, The elastic behavior of a crystalline aggregate: Proc. Phys. Soc. London, Ser. A, **65**, 349–359.
Hinz, K., Dostmann, H., and Fritsch, J., 1982, The continental margin of Morocco: Seismic sequences, structural elements, and geological development, *in* von Rad, U., Jinz, K., Sarrthein, J. M., and Seibold, E., Eds., Geology of the northwest African continental margin: Springer-Verlag.
Hurlbut, C. S., 1971, Dana's manual of mineralogy: Wiley.
Jachens, R. C., and Griscom, A., 1985, An isostatic residual gravity map of California—a residual map for interpretation of anomalies from intracrustal sources, *in* Hinze, W. J., Ed., The utility of regional gravity and magnetic anomaly maps: Soc. of Expl. Geophys.
Johnson, G. R., and Olhoeft, G. R., 1984, Density of rocks and minerals, *in* Carmichael, R. S., Ed., CRC handbook of physical properties of rocks, Volume II: CRC Press, 2–37.
Johnston, D. H., 1986, Shale properties at temperature and pressure: Oil and Gas J., 60–55.
Jones, T. D., 1986, Pore fluids and frequency-dependent wave propagation in rocks: Geophysics, **51**, 1939–1953.
Jones, T. D., and Nur, A., 1983, Velocity and attenuation in sandstone at elevated temperatures and pressures: Geophys. Res. Lett., **10**, 140–143.
Judd, W. R., and Shakoor, A., 1981, Density, *in* Touloukian, Y. S., and Ho, C. Y., Eds., Physical properties of rocks and minerals: McGraw Hill Data Series on Material Properties, Volume II-2: McGraw-Hill.
Kan, T. K., Batzle, M. L., and Gaiser, J. E., 1983, Attenuation measured from VSP, evidence of frequency dependent Q: presented at 53rd Ann. Internat. Mtg., Soc. Expl. Geophys.
Keenan, J. H., Keyes, F. G., Hill, P. G., and Moore, J. G., 1969, Steam tables: John Wiley and Sons.
Keller, G. R., Smith, R. A., Hinze, W. J., and Aikens, C. L. V., 1985, Regional gravity and magnetic study of West Texas, *in* Hinze, W. J., Ed., The utility of regional gravity and magnetic anomaly maps: Soc. of Expl. Geophys.
Kowallis, B., Jones, L. E. A., and Wang, H. F., 1984, Velocity-porosity-clay content systematics of poorly consolidated sandstones: J. Geophys. Res., **89**, 10355–10364.
Krynine, P. D., 1948, The megascopic study of field classification of sedimentary rocks: Jour. Geol., **56**, 130–165.
Kuster, G. T., and Töksoz, N. M., 1974, Velocity and attenuation of seismic waves in two-phase media, I. Theoretical formulations: Geophysics, **39**, 607–618.
Matthews, J. C., and Matthews, W. R., 1985, Program calculates frac gradients for many basins: Oil and Gas Journal.
Mavko, G. M., and Nur, A., 1977, The effect of nonelliptical cracks on the compressibility of rocks: J. Geoph. Res., **84**, 4769–4776.
McCulloh, T. H., 1967, Mass properties of sedimentary rocks and gravimetric effects of petroleum and natural gas reservoirs: U.S. Geol. Surv., Prof. Pap., 528 A.
McDonal, F. J., Angona, F. A., Mills, R. L., Sengbush, R. L., Van Nostrand, R. G., and White, J. E., 1958, Attenuation of shear and compressional waves in Pierre Shale: Geophysics, **23**, 421–439.
McSkimin, H. J., Andreatch, P., Jr., and Thurston, R. N., 1965, Elastic moduli of quartz vs. hydrostatic pressure at 25° and −195.8°C: J. Appl. Phys., **36**, 1632.
Milholland, P., Manghnani, M. H., Schlanger, S. O., and Sutton, G. H., 1980, Geoacoustic modeling of deep-sea carbonate sediments: J. Acoust. Soc. Am., **68**, 1351–1360.
Millero, F. J., Ward, G. K., and Chetirkin, P. V., 1977, Relative sound velocities of sea salts at 25°C: J. Acoust. Soc. Am., **61**, 1492.
Murphy, W. F., III, 1982, Effects of microstructure and pore fluids on acoustic properties of granular sedimentary materials: Ph.D. thesis, Stanford Univ.
Nur, A., and Simmons, G., 1969, The effect of viscosity of a fluid phase on velocity in low porosity rocks: Earth and Planetary Sci. Lett., **7**, 99–108.
O'Connell, R. J., and Budiansky, B., 1974, Seismic velocities in dry and saturated cracked solids: J. Geophy. Res., **79**, 5412–5426.
Pettijohn, F. S., 1975, Sedimentary Rocks: Harper and Row.
Pickett, G. R., 1963, Acoustic character logs and their applications in formation evaluation: J. Petr. Tech., **15**, 650–667.
Potter, R. W., and Brown, D. L., 1977, The volumetric properties of sodium chloride solutions from 0 to 500°C at pressures up to 2000 bars based on a repression of available data in the literature: U.S. Geol. Surv. Bull. 1421-C.
Rafavich, F., Kendal, C. H., St. C., and Todd, T. P., 1984, The relationship between acoustic properties and the petrographic character of carbonate rocks: Geophysics, **49**, 1622–1636.
Rao, K. S., and Rao, B. R., 1959, Study of temperature variation of ultrasonic velocities in some organic liquids by modified fixed-path interferometer method: J. Acoust. Soc. Am., **31**, 439–441.
Raymer, L. L., Hunt, E. R., Gardner, J. S., 1980, An improved sonic transit-time-porosity transform: Soc. Prof. Well Log Analysts, 21st Annual Logging Symposium Transactions, Paper P.
Rieke, H. H., and Chilingarian, G. V., 1974, Compaction of argillaceous sediments: Elsevier.
Rowe, A. M., and Chou, J. C. S., 1970, Pressure-volume-temperature-concentration relation of aqueous NaCl solutions: J. Chem. Eng. Data, **15**, 61–66.
Russell, W. L., 1951, Principles of petroleum geology: McGraw-Hill.
Schlumberger Inc., 1986, Log interpretation charts: Schlumberger, Inc.
Sergeev, L. A., 1948, Ultrasonic velocities in methane saturated oils and water for estimating sound reflectivity of an oil layer: 4th All-Union Acoust. Conf. Izd. Nauk SSSR.
Shaw, D. B., and Weaver, C. E., 1965, The mineralogical composition of shales: J. Sed. Petrology, **35**, 213–222.
Simmons, G., 1965, Ultrasonics in geology: Proc. IEEE, **53**, 1337–1345.
Simmons, G., and Brace, W. F., 1965, Comparison of static and dynamic measurements of compressibility of rocks: J. Geophys. Res., **70**, 5649–5656.
Spencer, J. W., 1981, Stress relaxation at low frequencies in

fluid saturated rocks: attenuation and modulus dispersion: J. Geophys. Res., **86B-3**, 1803–1812.
Standing, M. B., 1962, Oil-system correlations, *in* Frick, T. C., Ed., Petroleum production handbook Volume II, Part 19: McGraw-Hill.
Stoll, R. D., and Houtz, R. E., 1983, Attenuation measurements from sonoboys: J. Acoust. Soc. Am., **73**, 163–172.
Storer, D., 1959, Compaction of the argillaceous sediments in the Padano Basin, *in* The gasiferous deposits of Western Europe, 2: Acad. Nazl. dei Lincei, Roma, 519–536.
Sultanov, R. G., Skripka, V. G., and Namiot, A. Y., 1972, Solubility of methane in water at high temperatures and pressures: Gazovaia Promyshlenmost, 17 (May), 6–7.
Terzaghi, K., and Peck, R. B., 1948, Soil mechanics in engineering practice: Wiley.
Thomas, L. K., Hankinson, R. W., and Phillips, K. A., 1970, Determination of acoustic velocities for natural gas: J. Pet. Tech., **22**, 889–892.
Thomsen, L., 1986, Weak elastic anisotropy: Geophysics, **51**, 1954–66.
Timur, A., 1977, Temperature dependence of compressional and shear wave velocities in rocks: Geophysics, **42**, 950–956.
Töksoz, M. N., and Johnston, D. H., 1981, Seismic wave attenuation: Soc. Expl. Geophys.
Tosaya, C. A., 1982, Acoustical properties of clay-bearing rocks: Ph.D. Thesis, Stanford Univ.
Tullos, F. N., and Reid, A. C., 1969, Seismic attenuation of Gulf Coast sediments: Geophysics, **34**, 516–528.
Volarovich, M. P., Bayuk, E. I., and D'Yaur, J. J., 1985, Change in the velocity of longitudinal waves during deformation of samples: Izvestiya, Earth Physics, **21**, 302–304.
Wang, Z. J., and Nur, A., 1986, The effect of temperature on the seismic wave velocities in rocks saturated with hydrocarbons: SPE paper 15646, Proc. 61 Mtg. Soc. Pet. Eng.
Wang, Z. J., Nur, A. M., and Batzle, M. L., 1988, Acoustic velocities in petroleum oils: SPE paper 18163, Proc. 63 Mtg. Soc. Pet. Eng., 571–584.
Watt, J. P., Davies, G. F., and O'Connell, R. J., 1976, The elastic properties of composite materials: Rev. Geophys. and Space Physics, **14**, 541–563.
White, J. E., 1983, Underground sound: Application of seismic waves: Elsevier.
Wilkins, R., Simmons, G., and Caruso, L., 1984, The ratio V_p/V_s as a discriminant of composition for siliceous limestones: Geophysics, **49**, 1850–1860.
Wilson, W. D., 1959, Speed of sound in distilled water as a function of temperature and pressure: J. Acoust. Soc. Am., **31**, 1067–1072.
Winkler, K. W., 1986, Estimates of velocity dispersion between seismic and ultrasonic frequencies: Geophysics, **51**, 183–189.
Wood, A. B., 1941, A textbook of sound: MacMillan.
Wyllie, M. R. J., Gregory, A. R., and Gardner, L. W., 1956, Elastic wave velocities in heterogeneous and porous media: Geophysics, **21**, 41–70.
Zarembo, V. I., and Fedorov, M. K., 1975, Density of sodium chloride solutions in the temperature range 25-350°C at pressures up to 1000 kg/cm^2: J. Appl. Chem. USSR, **48**, 1949–1953, (English translation).